

# Survey of ion plasma parameters in Saturn's magnetosphere

M. F. Thomsen,<sup>1</sup> D. B. Reisenfeld,<sup>2</sup> D. M. Delapp,<sup>1</sup> R. L. Tokar,<sup>1</sup> D. T. Young,<sup>3</sup>  
F. J. Crary,<sup>3</sup> E. C. Sittler,<sup>4</sup> M. A. McGraw,<sup>2,5</sup> and J. D. Williams<sup>2</sup>

Received 11 January 2010; revised 5 May 2010; accepted 13 May 2010; published 9 October 2010.

[1] A survey of the bulk plasma ion properties observed by the Cassini Plasma Spectrometer instrument over roughly the first 4.5 years of its mission in orbit around Saturn is presented. The moments (density, temperature, and flow velocity) of the plasma distributions below 50 keV have been computed by numerical integration of the observed counts in the “Singles” (non-mass-resolved) data, partitioned into species on the basis of concurrent determinations of the composition from the time-of-flight data. Moments are presented for three main species: H<sup>+</sup>, W<sup>+</sup> (water group ions), and ions with  $m/q = 2$ , which are presumed to be H<sub>2</sub><sup>+</sup>. While the survey extends to radial distances of 30  $R_S$  and thus includes some solar wind or magnetosheath values, our principal interest is the large-scale spatial variation of the magnetospheric plasma properties, so we focus attention on radial distances inside of 17  $R_S$ . Principal findings include the following: (1) the densities of all three components are highly variable but are generally well organized by dipole  $L$  and magnetic latitude; (2) the density of ions with  $m/q = 2$  varies from a few percentage of the H<sup>+</sup> density in the inner magnetosphere to a maximum of several tens of percentage near the orbit of Titan, suggesting that Titan is an important source for H<sub>2</sub><sup>+</sup> in the outer magnetosphere; (3) water group ions are the dominant population in the inner magnetosphere, but only within  $\sim 3 R_S$  of the equatorial plane because of their strong centrifugal confinement; (4) derived latitudinal scale heights are largest for the light ions and generally increase with radial distance; (5) the  $L$  dependence of the calculated temperatures is not consistent with adiabatic transport but is in fair agreement with the expectations for plasma originating from ion pickup; (6) in agreement with the findings of Sergis et al. (2010), inside of  $L \sim 11$ , the particle pressure is dominated by ions with energies below a few keV; (7) the derived flow velocities reveal the global circulation pattern of relatively dense populations in the magnetosphere, with no evidence for return circulation from the nightside to the dayside beyond  $\sim 20 R_S$ ; and (8) the azimuthal flow speeds are typically less than full corotation over the entire  $L$  range examined, varying from  $\sim 50\%$  to 70% of full corotation.

**Citation:** Thomsen, M. F., D. B. Reisenfeld, D. M. Delapp, R. L. Tokar, D. T. Young, F. J. Crary, E. C. Sittler, M. A. McGraw, and J. D. Williams (2010), Survey of ion plasma parameters in Saturn's magnetosphere, *J. Geophys. Res.*, 115, A10220, doi:10.1029/2010JA015267.

## 1. Introduction

[2] Prior to 2004, Saturn's magnetosphere was visited 3 times by spacecraft: Pioneer 11 in 1979, Voyager 1 in 1980, and Voyager 2 in 1981, all of which were rapid flybys. Since mid-2004, the Cassini spacecraft has been in orbit around Saturn and, having now completed its 4 year prime mission, has entered an extended mission phase with continuing exciting scientific results. Each of the earlier

missions provided crucial information about the plasma distribution and dynamics in Saturn's magnetosphere, but by virtue of its multiple passes and continuous sampling over several years, Cassini is yielding vastly expanded spatial and temporal coverage of the magnetospheric properties. The purpose of this paper is to present a summary of some of the important plasma properties of Saturn's magnetosphere, as revealed by in situ ion observations from the Cassini Plasma Spectrometer (CAPS) during the first 4.5 years in Saturn orbit.

[3] Starting with Pioneer 11, which made (non-mass-resolved) ion measurements only above 100 eV, it was inferred that the plasma in Saturn's magnetosphere corresponded to several different ion species, the most plausible source being water group products, presumably originating from Saturn's inner satellites and rings [Frank et al., 1980].

<sup>1</sup>Los Alamos National Laboratory, Los Alamos, New Mexico, USA.

<sup>2</sup>University of Montana, Missoula, Montana, USA.

<sup>3</sup>Southwest Research Institute, San Antonio, Texas, USA.

<sup>4</sup>Goddard Space Flight Center, Greenbelt, Maryland, USA.

<sup>5</sup>Now at Tetra Tech, Missoula, Montana, USA.

The density of the plasma was largest and the temperature was lowest within the inner magnetosphere, and the plasma beta was found to exceed 1 beyond about  $6 R_S$ , suggesting the possibility of sporadic plasma loss through outflow to the magnetotail [Frank *et al.*, 1980]. The distribution of plasma flow was found to be dominantly in the corotational direction, at nearly the corotational speed in the inner magnetosphere, but falling below that beyond  $\sim 10 R_S$  [Frank *et al.*, 1980].

[4] The measurements of Voyagers 1 and 2 added considerably greater quantitative detail to the sketch drawn from the Pioneer flyby. A series of studies of the data and comparison with models yielded a fairly comprehensive description of the radial dependence of plasma parameters derived from the Voyager PLS (Plasma Science) instruments, plus important information about the latitudinal variations. These studies and their implications have been summarized by Richardson [1998].

[5] With its lower energy threshold (10 eV), the PLS was able to observe not only the heavy-ion component in the inner magnetosphere but also the  $H^+$  component, which fell below the energy range of the Pioneer 11 plasma instrument. The presence of two comoving ion species allowed less ambiguous fits to the observed energy/charge ( $E/q$ ) spectra, so in spite of the lack of mass-resolving capability, the Voyager plasma data enabled the identification of the heavy ions as  $N^+$  or  $O^+$  (the latter also including the other water group ions  $OH^+$ ,  $H_2O^+$ , and  $H_3O^+$ ). Since fits to the  $E/q$  spectra yielded lower  $\chi^2$  with  $O^+$  assumed than with  $N^+$  assumed, it was concluded that the heavy species was dominantly water group ions.

[6] The Voyager data, interpreted to be  $H^+$  and  $O^+$ , revealed that the densities of both species peaked in the inner magnetosphere near  $L \sim 5-7$ . The different latitudes covered by the inbound and outbound passes enabled the determination that inside  $L \sim 10$ , the densities fall off with latitude, especially for the  $O^+$ . Beyond  $L \sim 12-15$  and out to the magnetopause, Voyager found strong density variations. The inferred ion temperatures increased with radial distance out to  $L \sim 10$  and were quite variable beyond. The low-latitude temperatures appeared to be higher than at higher latitudes. In general, the temperatures of both species were comparable to the corresponding pickup energies for fresh ionization in a corotating magnetic field. The derived flow velocities were dominantly in the azimuthal (i.e., corotation) direction, but with a magnitude that was generally lower than strict corotation, especially beyond  $L \sim 6$ . Particularly in the outer magnetosphere, there were significant and quite variable nonazimuthal flow components, with a general tendency toward outward flow.

[7] With the arrival of Cassini at Saturn in July 2004, a new era of exploration of the plasma populations of Saturn's magnetosphere began. One of the biggest advances is that Cassini enabled the first mass-resolved measurements of Saturnian plasmas. With time-of-flight technology, the Cassini Plasma Spectrometer (CAPS) has unambiguously confirmed that  $H^+$  and water group (hereafter designated  $W^+$ ) ions are the dominant constituents of Saturn's magnetospheric plasma [Young *et al.*, 2005]. In addition, other less prominent species have been identified, including  $O_2^+$  [Young *et al.*, 2005; Tokar *et al.*, 2005] and  $N^+$  [Young *et al.*, 2005; Smith *et al.*, 2005, 2007]. The identification of  $H_2^+$  was

mentioned in passing by Sittler *et al.* [2005], and although it has not received much attention to date, our results below demonstrate that it is actually a significant fraction of the total density, particularly in the outer magnetosphere.

[8] The other major advance enabled by Cassini is the possibility of multiple passes through different spatial regions (high latitude as well as equatorial) of the magnetosphere, increasing our ability to distinguish spatial and temporal variations in the plasma properties. For example, using a careful forward-modeling analysis of CAPS data, Wilson *et al.* [2008] have examined the plasma densities, temperatures, and flow velocities from five suitable passes through the inner magnetosphere (between 5.5 and  $11 R_S$ ). Fitting only to the dominant species  $H^+$  and  $W^+$ , they found only modest variability in the plasma properties from pass to pass, with values similar to those derived by Sittler *et al.* [2005, 2008] from the first pass through the region during Saturn Orbit Insertion. McAndrews *et al.* [2009] used the same type of analysis to explore flow velocities observed throughout the nightside magnetosphere on 35 days between October 2005 and May 2007. While there were clear variations from pass to pass and even within individual passes, a rather coherent global flow pattern nonetheless emerged.

[9] The purpose of the present analysis is to summarize the bulk plasma ion properties observed by the Cassini CAPS instrument over roughly the first 4.5 years of the mission. As discussed more completely below, we employ the moments (density, temperature, flow velocity) of the plasma distributions, computed by numerical integration of the observed counts in the Singles (non-mass-resolved) data, partitioned into species on the basis of concurrent determinations of the ion composition from the time-of-flight data. The objective is to perform a broad-brush global survey of the plasma parameters using these easily computed moments, with the aim of identifying the large-scale spatial variation of the magnetospheric plasma properties. We emphasize that the "major" ion species reported on here dominate the magnetospheric plasma physics and that minor species (e.g., in most cases,  $N^+$ ) while, interesting for other reasons, do not critically affect the plasma dynamics.

## 2. Instrument and Observations

[10] The Cassini CAPS instrument has been described in detail by Young *et al.* [2004]. For the present study, data from the ion mass spectrometer (IMS) element of CAPS are used. The IMS consists of a top-hat electrostatic analyzer for  $E/q$  determination, followed by a time-of-flight analyzer for determination of ion velocity, and hence mass-per-charge ( $m/q$ ) determination. The plate voltage on the electrostatic analyzer is swept every 4 s to cover the nominal  $E/q$  range of 1–50 keV in 64 logarithmically spaced bins. Time of flight is measured by the detection of a "start" electron liberated from a thin carbon foil as the incident ion passes through, in coincidence with a "stop" detection of the emerging ion (or its neutralized counterpart) after traversing a flight path of 18.8 cm. The start-only signals (the so-called singles, SNG, data product) are monitored separately from the coincidences, yielding a higher detection efficiency but no mass determination.

[11] The start anode of the time-of-flight section has a position-sensitive readout that enables the direction of

motion of detected particles to be identified and binned in  $20^\circ$  segments. In the orthogonal direction, particle velocities are sampled by an actuator that physically rotates the instrument so that the planar field-of-view covers between  $-80^\circ$  and  $+104^\circ$  relative to the direction that is radially outward from the spacecraft (the spacecraft  $-y$  axis). Since Cassini is three-axis stabilized, the actuator enables CAPS to view approximately  $2\pi$  steradians at any given time ( $4\pi$  steradians can be observed in combination with spacecraft rotation, but over a longer time period,  $\sim 30$  min). The specific range of angles viewed during a given accumulation interval depends on the intrinsic angular acceptance of the analyzer and the rate of actuation, which is nominally  $1^\circ/\text{s}$  but is slower near the turning points of the actuation range. It also depends on the telemetry rate, because at lower rates, data from adjacent azimuthal (i.e., actuation) angles must be summed to reduce the overall data volume for a given spectrum. At the highest telemetry rates, a single measurement of the SNG count rate covers an angular bin of approximately  $20^\circ$  in polar angle by  $8^\circ$  in azimuth (the intrinsic angular resolution of the instrument), repeated every 4 s energy sweep (approximately  $4^\circ$ ). At lower rates, the azimuthal angle coverage in a single measurement is  $12^\circ$  or even  $20^\circ$  because of the need to sum adjacent sweeps.

[12] In principle, mass-binned measurements from the TOF determination are taken with the same cadence as the SNG data, but telemetry restrictions severely limit the amount of time that such mass- and angle-resolved distributions can be returned. On the other hand, for most telemetry rates, a TOF spectrum consisting of angle-integrated (summed over detectors and azimuths) counts versus  $E/q$  and time-of-flight bin is returned. This TOF spectrum allows us to partition the counts in the corresponding SNG data into different mass bins, on the assumption that all species have roughly the same angular distribution. This combination allows us to take advantage of the much greater SNG coverage and statistics while still exploiting the mass-determination capabilities of the IMS. The method by which this partition is accomplished is described in Appendix A.

[13] From the species-partitioned SNG counts observed as a function of  $E/q$ , polar angle (i.e., anode), and actuator angle, the basic moments of the distribution (density, flow velocity, and temperature) are calculated for each species using an automated “production” code. The approach used for this numerical integration is briefly described in Appendix B. A more complete description is presented by Thomsen and Delapp [2005] (this report is available at [http://nis-www.lanl.gov/nis-projects/caps/Moments\\_Computation.pdf](http://nis-www.lanl.gov/nis-projects/caps/Moments_Computation.pdf)). Automation of the moments code was an important step that allows us to reduce the large quantities of data needed for a survey such as this. However, the algorithm used for the computation has several shortcomings that limit its applicability to only certain conditions: One problem is that the background counts due to penetrating charged particles are not adequately removed from the observed SNG rates, producing inaccuracies in the moments derived in the inner magnetosphere (inside of  $L = 5$  or 6). In this region also, the spacecraft surface potential can be several volts negative, and the assumption in the production moments code that the potential is  $-3$  V can lead to significant errors in the derived values, particularly for the low-mass species.

In addition, the current production code does not properly account for the spacecraft roll in determining the detector look directions, so only data from nonrolling intervals are deemed suitable for the present study. These deficiencies will be corrected in a future revision of the numerical algorithm, but for the time being, we restrict our attention to nonrolling intervals, and we view with caution any results from inside about  $L = 6$ .

[14] A more fundamental limitation of the data we use for this study arises from the fact that Cassini is three-axis stabilized, which prevents CAPS from viewing the entire  $4\pi$  steradians of the sky (except on the few occasions when the spacecraft is rolling, which are not included in this study, as just mentioned). As reported by numerous authors previously [e.g., Richardson, 1998, and references therein; Sittler *et al.*, 2005, 2006, 2008; Wilson *et al.*, 2008], the thermal ion populations in Saturn's magnetosphere typically have a flow speed that is comparable to their thermal speed. For these trans-sonic conditions, a detector must look into the flow in order to observe the complete distribution. If the flow does not lie within the instrument field of view, few counts will be observed, and erroneous moments will be calculated. This viewing problem has been discussed in some detail by Wilson *et al.* [2008] and McAndrews *et al.* [2009], and for those studies only measurements satisfying a very restrictive set of conditions were accepted. Since those conditions were not imposed during the calculation of the production numerical moments used for the present study, we approach this viewing problem from a different perspective, using all derived values (with the exceptions noted above) and applying different filters to the results as described below.

[15] As explained in Appendix A, the SNG data are partitioned into three species based on concurrent TOF data. The three species are  $\text{H}^+$  ( $m/q = 1$ ),  $\text{H}_2^+$  or  $\text{He}^{2+}$  ( $m/q = 2$ ), and  $\text{W}^+$  (comprising  $\text{O}^+$ ,  $\text{OH}^+$ ,  $\text{H}_2\text{O}^+$ , and  $\text{H}_3\text{O}^+$ , with  $m/q$  from 16 to 19). The justification for this selected set of species is presented in Figure 1, which shows typical energy versus time-of-flight spectra from two locations within the magnetosphere. Figure 1a was obtained between  $L = 12.04$  and  $L = 12.89$ , while the Figure 1b was obtained between  $L = 6.47$  and  $L = 7.00$ , both on 11 October 2005. Aside from some “ghost peaks” attributable to scattering within the instrument, the most prominent peaks are labeled according to the parent species. Within the peaks labeled “ $\text{W}^+$ ,” there may also be a small contribution from  $\text{N}^+$ , but this population has previously been extensively addressed by Smith *et al.* [2005, 2007] and will not be considered here. Moreover, its presence will not affect the bulk plasma properties in any significant way. In Figure 1, the peaks labeled “ $\text{H}_2^+$ ” could also be due to  $\text{He}^{2+}$ , and we do not have a ready way to distinguish between them (both have  $m/q = 2$ , and IMS is a mass/charge spectrometer). However, given the strong preponderance of water group ions in the inner magnetosphere, there is a good theoretical basis for expecting  $\text{H}_2^+$  to be there in significant numbers [e.g., Richardson *et al.*, 1986]. Moreover, at somewhat higher energies than CAPS attains (83–223 keV/ $q$ ), measurements from the MIMI instrument on Cassini suggest that in the radial range of 5.7–12.6  $R_{\text{S}}$ , only  $\sim 5\%$  of the ions with  $m/q = 2$  are  $\text{He}^{2+}$  [Krimigis *et al.*, 2005]. Theory also predicts that Titan is a

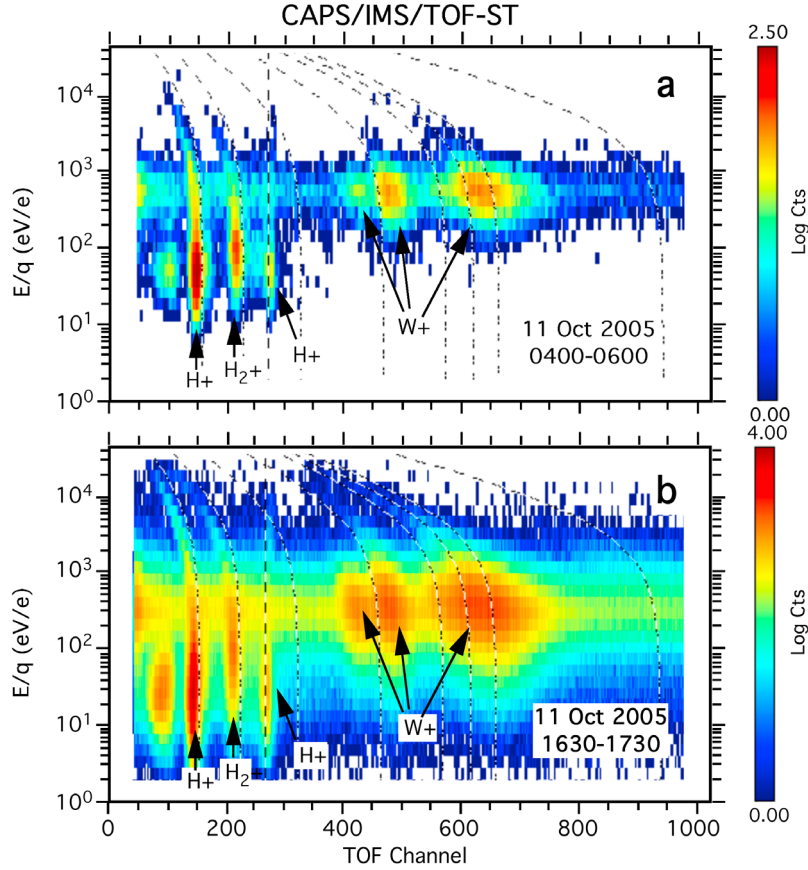


**Figure 1.** Energy-per-charge versus time-of-flight spectrograms from the CAPS/IMS straight-through spectrometer. Various ion species occupy characteristic regions of the spectrogram, as labeled. Measurements were obtained (a) between  $L = 12.04$  and  $L = 12.89$  in the middle magnetosphere and (b) between  $L = 6.47$  and  $L = 7.00$  in the inner magnetosphere, both on 11 October 2005.

significant source of  $H_2^+$  in the outer magnetosphere [Cui *et al.*, 2008].

[16] The data used in the present study cover the interval from 26 October 2004 (the first Cassini passage through the magnetosphere when the CAPS actuator was operating) through 31 March 2009. The production moments have been filtered so that the following conditions are met:

[17] 1. actuator operating;

[18] 2. spacecraft not rolling; and

[19] 3. successful iteration in moments calculation (see Appendix B).

[20] The result of applying these conditions is a total of ( $1.19 \times 10^5$ ,  $1.22 \times 10^5$ , and  $1.33 \times 10^5$ ) moments values for the three species  $H^+$ ,  $H_2^+$ , and  $W^+$ , respectively. Low count rates, primarily from bad viewing or a spacecraft location in the low-density lobes, further reduce the number of usable values (defined as nonzero densities returned by the partition algorithm from the TOF data) to 48,847, 38,664, and 57,408 for the three species, respectively. Figure 2 shows the  $x$ - $y$  and  $x$ - $z$  plane projections of the spatial coverage for nonzero densities for each of the three species where these conditions are satisfied. Figure 2 uses the Saturn solar equatorial coordinate system (referred to as SZS by some researchers, a designation we will follow here), which has

the  $z$  axis aligned with Saturn's rotational axis, the  $x$  axis perpendicular to that in the plane containing the rotational axis and the Saturn-Sun direction (positive toward the Sun), and the  $y$  axis completing the set, positive in the dusk direction. As Figure 2 shows, local time coverage is generally good, except in the postdusk outer magnetosphere. Also, nonzero  $W^+$  determinations are quite sparse throughout the magnetotail [see also McAndrews *et al.*, 2009].

[21] In the following sections, we will place our statistical results into the context of the results reported by other authors. We have also done event-by-event comparisons with the densities derived by other means. In particular, we have compared our total ion densities (i.e., the sum of the densities for the three species) with the published electron densities derived from CAPS/ELS data [Arridge *et al.*, 2009, Figure 1; Schippers *et al.*, 2008, Figure 3], from the upper hybrid line determination of RPWS [Schippers *et al.*, 2008, Figure 3], and from the Langmuir probe on RPWS [Morooka *et al.*, 2009, Figure 3a]. In each comparison, when CAPS viewing is appropriate and there are sufficient ion counts to successfully obtain moments, we find very reasonable agreement. The time resolution of the electron density determinations is typically higher than that for the ions, and the electron density generally exhibits more

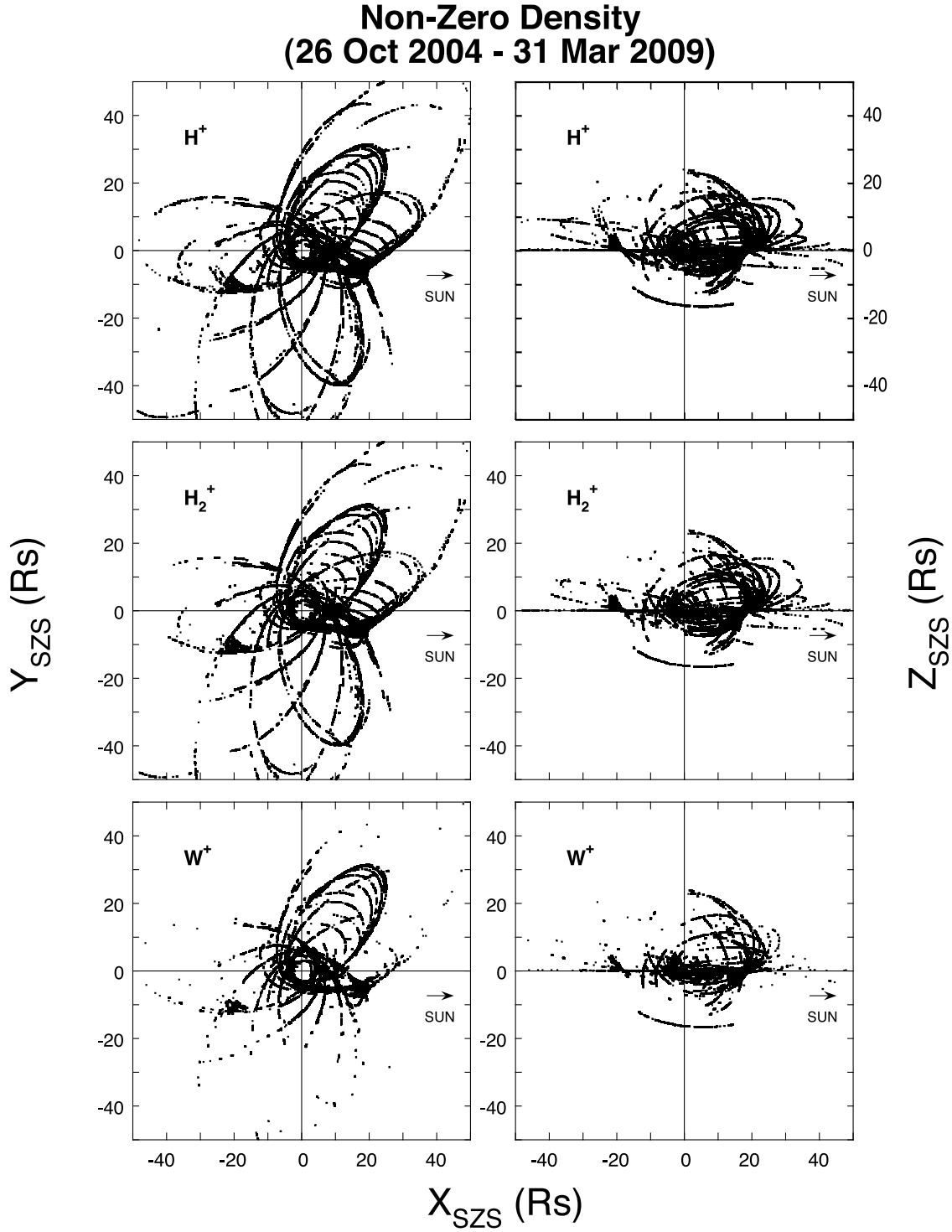


**Figure 2.** SZS (left)  $x$ - $y$  and (right)  $x$ - $z$  plane projections of coverage for densities between 26 October 2004 and 31 March 2009. From top to bottom, the three species are  $H^+$ ,  $H_2^+$  ( $m/q = 2$ ), and  $W^+$ . The SZS coordinate system has the  $z$  axis aligned with Saturn's rotational axis, the  $x$  axis perpendicular to that in the plane containing the rotational axis and the Saturn-Sun direction (positive toward the Sun), and the  $y$  axis completing the set, positive in the dusk direction.

temporal structure, but our derived ion densities tend to follow rather well the smoothed profiles. Agreement with the RPWS density in the inner magnetosphere [Schippers et al., 2008] is to within  $\sim 20\%$ . Agreement with the

Langmuir probe data [Morooka et al., 2009] is generally better than a factor of 2, with no systematic differences seen. Although the Arridge et al. events were characterized by quite low densities so that only one had enough ion counts for even

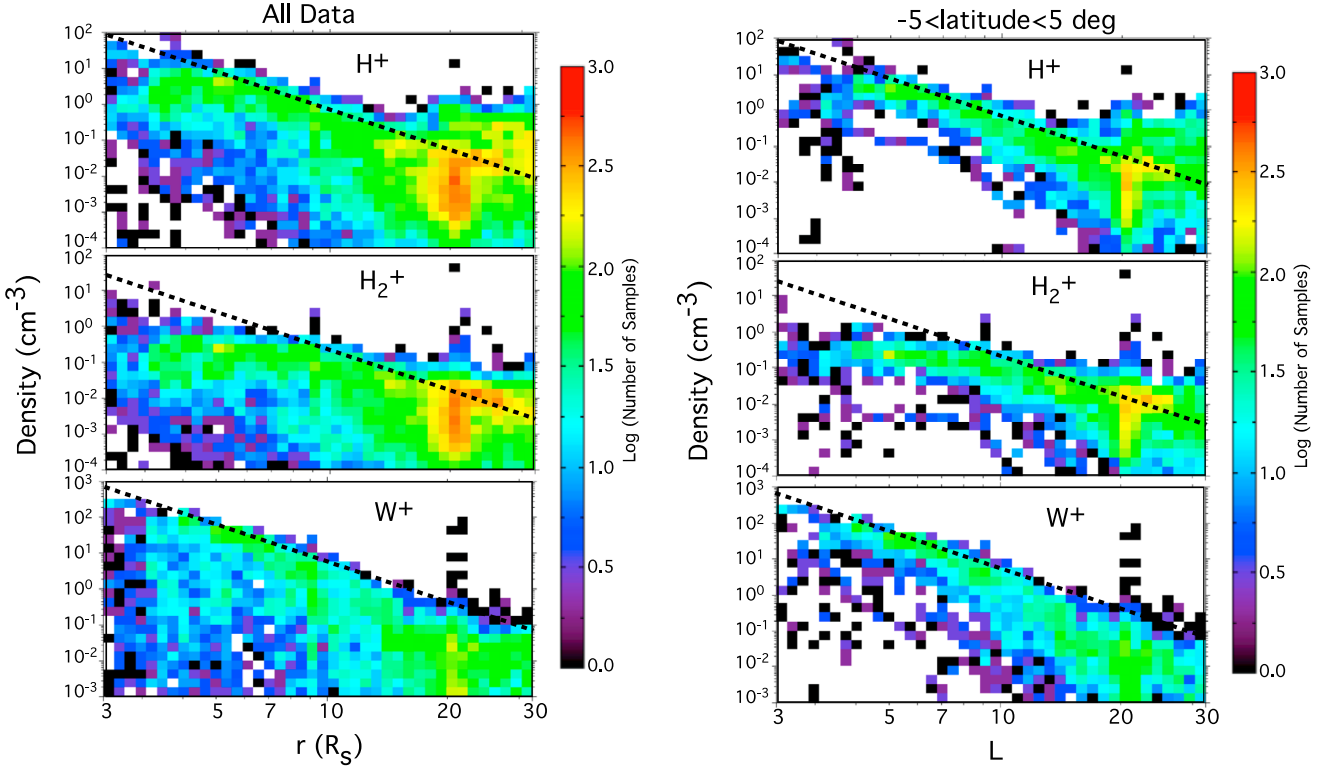


**Figure 3.** (a) Occurrence distribution of derived densities for the three ion species (top,  $H^+$ ; center,  $H_2^+$ ; bottom,  $W^+$ ) as a function of radial distance from Saturn for the full set of data meeting the constraints that the actuator was actuating, the spacecraft was not rolling, and the iteration in the moments calculation was successful. The data have been sorted into density and radial distance bins, with the number of samples in each bin color-coded. The dashed lines represent estimated upper bounds for the distribution of values. (b) Same as in Figure 3a, but with the additional constraint that the latitude is within  $\pm 5^\circ$  of the equatorial plane, and the data are plotted as a function of  $L$  instead of  $r$ . The dashed lines are the same functions as illustrated in Figure 3a, with  $L$  substituted for  $r$ . (c) Same as in Figure 3b, but with the additional constraint that only points for which the corotation direction is within the CAPS field of view are included. The large black dots show the means for the values within  $1-R_S$   $L$  bins and are plotted at the center of each bin. The dashed lines in the top and bottom frames are the formulas reported by Wilson et al. [2008] for a carefully selected set of forward-modeling results in the inner magnetosphere.

a few successful determinations, the ion densities for that event lay in the center of the more-variable electron densities.

### 3. Results and Discussion

#### 3.1. Densities

[22] In this section, we explore the spatial dependence of the derived densities for the three species. We begin by displaying the full set of data satisfying the criteria described above, and then we progressively narrow the data set to extract the physically meaningful dependences.

[23] Figure 3a shows, as a function of radial distance, the densities derived for the three species for spectra meeting the above criteria. The data have been sorted into bins in density and radial distance, and Figure 3a shows the color-coded number of samples in each bin. Since we have not placed any constraints on the viewing, these plots include measurements where the flow was well inside the CAPS field of view, as well as measurements where it was partially or completely outside of the field of view. This, plus the

range of latitude included in this data set and the fact that we have not filtered out magnetosheath data at larger radial distances, accounts for the large amount of scatter in the derived values for the density. On the assumption that the largest densities observed over time are likely to be those when CAPS was viewing the entire distribution, we focus on the upper bound of derived values. For the  $H^+$  (top) it appears that an  $r^{-4}$  dependence describes fairly well the radial variation of this upper bound over a radial range from  $\sim 6 R_S$  out to the magnetopause somewhere at or beyond  $\sim 18 R_S$ , where the typical density jumps up as the magnetosheath plasma is encountered. The rough upper bound for  $H^+$  plotted as a solid line at the top of Figure 3a is  $8100 \cdot r^{-4} \text{ cm}^{-3}$ , with  $r$  in units of  $R_S$ .

[24] Figure 3a (center) shows that  $r^{-4}$  is a reasonable representation of the upper bound on the density of ions with  $m/q = 2$  beyond  $\sim 9 R_S$ , but inside of that distance, the density bound seems flat at  $\sim 0.4 \text{ cm}^{-3}$ . The estimated upper bound from  $r \sim 9 R_S$  out to the magnetopause is  $2430 \cdot r^{-4} \text{ cm}^{-3}$ . The apparent increase in  $m/q = 2$  densities at the magneto-

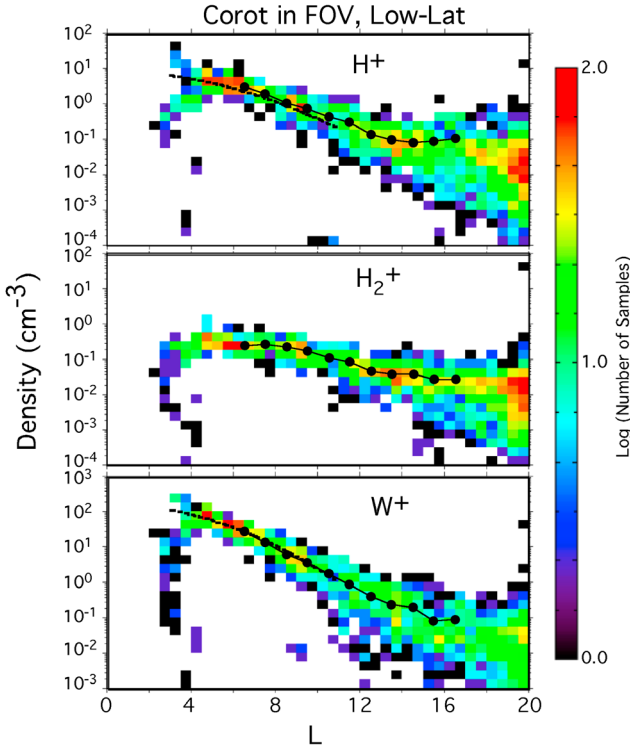


**Figure 3.** (continued)

pause is less evident than for  $H^+$ , with the consequence that the ratio of  $m/q = 2$  to  $H^+$  ions may be a reasonably good marker for magnetosheath material in the outer magnetosphere, as discussed further below.

[25] Figure 3a (bottom) shows that  $r^{-4}$  is also a reasonable representation of the upper bound on the density of water group ions between  $\sim 5$  and  $12 R_S$ , where the expression for the dashed curve is  $61,600 \cdot r^{-4} \text{ cm}^{-3}$ .

[26] Figure 3b is the same as Figure 3a, except that we have imposed the additional constraint that only measurements obtained within  $\pm 5^\circ$  of the equatorial plane are included, and we have plotted the data as a function of  $L$  instead of  $r$ . (The choice of  $\pm 5^\circ$  defines a near-equatorial region that is everywhere less than half the latitudinal scale heights derived for all three species, as presented below. Nearly identical results are obtained if we instead define “near-equatorial” as  $|z| < 0.5 R_S$ .) Restricting the data to near-equatorial locations removes many of the low values evident in Figure 3a, and the remaining points tend to lie close to the upper bounds identified in Figure 3a (expressed now in terms of  $L$  instead of  $r$ ). There nonetheless remain a significant number of points that lie well below those bounds, which may be attributable to the fact that the flow may not be in the CAPS field of view.

[27] In Figure 3c, we again show all the measurements that are within  $\pm 5^\circ$  of the equator, but with the additional requirement that the instrument field of view should include the direction of corotation, which is shown below to be the dominant flow direction. The binned data are shown now as a linear function of  $L$ , out to only  $L = 20$ . Also shown in

Figure 3c, as the solid black dots are the mean densities in  $1 R_S L$  bins. The median values could also have been presented, but they only differ significantly from the means for  $W^+$  in the outer magnetosphere. It is clear that restricting attention to near-equatorial measurements and good viewing for corotation eliminates many of the low-density values seen in Figures 3a and 3b. For comparison, Figure 3c also shows the density profiles reported by Wilson et al. [2008] for  $H^+$  and  $W^+$ , valid only at the equator and inside  $r \sim 11 R_S$ , as the black dashed curves. Over the range of validity of our different analyses, there is excellent agreement between the production numerical moments and the hand-selected, forward-modeling results.

[28] To obtain a quantitative description of the low-latitude radial dependence of the densities, we have fit the means from the various  $L$  bins shown in Figure 3c with power law and exponential functions of  $L$ , with the results shown in Table 1. Table 1 also includes fits to the total density obtained by summing the three species. Both power law and exponential fits provide a reasonably good representation of the  $L$  dependence of the bin means. These fits are in good agreement with the equatorial densities inferred by Persoon et al. [2009] (not shown): The exponential fit for  $W^+$  from Table 1 varies by less than 20% from the  $W^+$  densities presented by Persoon et al. over the range of overlap of the two studies ( $L = 6 - 10$ ). The power law fit for the  $H^+$  densities in Table 1 agrees similarly well with the Persoon et al. values near  $L = 6 - 7$  and  $L = 9 - 10$ , but it shows no evidence of the pronounced peak Persoon et al. found between  $L = 7$  and  $8$ . The fit to the combined densities of the three species shown in Table 1 yields a variation with radial distance that lies well between the upper and lower limits reported by Morooka et al. [2009].

### 3.2. Composition

[29] Figure 4 shows the ratio of the densities for the different species for those samples where nonzero densities were calculated for both  $H^+$  and  $m/q = 2$  (top) or both  $H^+$  and  $W^+$  (bottom). We have again restricted attention to low latitudes (within  $\pm 5^\circ$  of the equatorial plane) and to conditions where the corotation direction is within the CAPS field of view. Figure 4 (top) shows that the density of  $H_2^+$  (or possibly  $He^{2+}$  in the outer magnetosphere) tracks the  $H^+$  density fairly well, with values of several percent in the inner magnetosphere, rising to several tens of percent in the outer magnetosphere and tail. Beyond  $17 R_S$ , there is a bimodal distribution of values, with the lower values (a few percent) corresponding to magnetosheath/solar wind, where the ions with  $m/q = 2$  are certainly  $He^{2+}$ . Low values of this

**Table 1.**  $L$  Dependence of Low-Latitude Mean Densities in  $1-R_S$   $L$  Bins ( $6 < L < 17$ )

Parameter	$H^+$	$H_2^+$	$W^+$	Total Ions
<i>Exponential Fit</i>				
$A$	29.5	1.72	1166	627
$B$	0.387	0.268	0.607	0.517
Corr. Coeff.	0.994	0.948	0.997	0.991
<i>Power Law Fit</i>				
$C$	$1.01 \times 10^4$	79.7	$8.72 \times 10^6$	$1.38 \times 10^6$
$m$	4.28	2.88	6.62	5.68
Corr. Coeff.	0.993	0.895	0.993	0.998

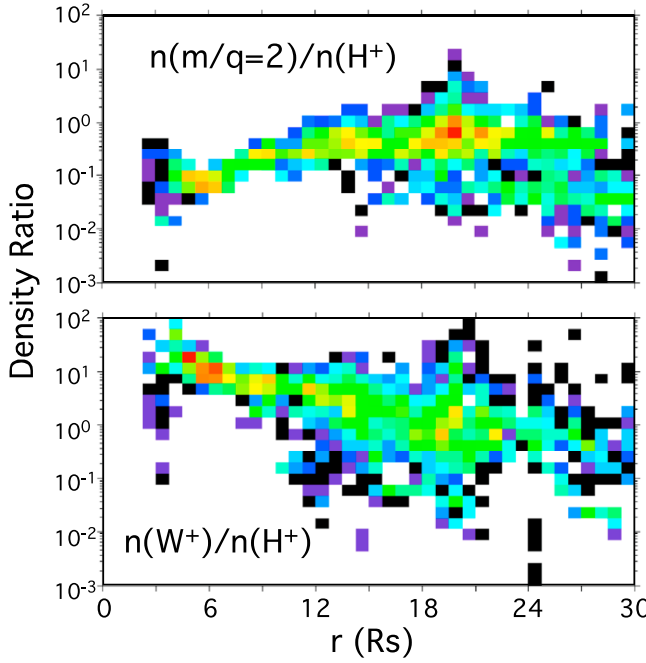


**Figure 4.** Occurrence distribution of the ratio of densities of ions with (top)  $m/q = 2$  and (bottom)  $W^+$  to  $H^+$  as a function of radial distance. The relative abundance of  $m/q = 2$  ions varies systematically from a few percent in both the inner magnetosphere and the solar wind/magnetosheath to a maximum of several tens of percent near  $20 R_S$ . The relative abundance of  $W^+$  is more variable but shows a general decline of more than an order of magnitude from the inner to the outer magnetosphere. Only measurements within  $\pm 5^\circ$  of the equatorial plane and for which the corotation direction lies within the field of view are included. The observed scatter is attributable to the influence of a number of parameters (e.g., longitude, local time, boundary crossings, temporal variability).

density ratio may thus be a good marker for solar wind material within the outer magnetosphere, a topic to explore in future work. It is noteworthy that in the outer magnetosphere and tail, ions with  $m/q = 2$  constitute a significant contribution to the total ion density. The fact that the ratio of  $m/q = 2$  to  $H^+$  in the outer magnetosphere exceeds its value in the solar wind by an order of magnitude or more is strong evidence that the solar wind is not the primary source of the plasma in this region and justifies our labeling this population as  $H_2^+$  within the magnetosphere. It is also noteworthy that the maximum ratios of  $H_2^+$  to  $H^+$  occur in the region near Titan's orbit ( $20.2 R_S$ ), which suggests that Titan may well be an important source for  $H_2^+$  in the outer magnetosphere [Cui et al., 2008].

[30] Figure 4 (bottom) shows that the  $W^+$  density is less well correlated with the  $H^+$  density than is the  $H_2^+$  density. This may be primarily due to the strong equatorial confinement of the heavy ions in the centrifugal potential well [e.g., Sittler et al., 2008], as is shown in the bottom of Figure 5. Figure 5 shows that the  $W^+$  density dominates over the  $H^+$  density only within  $\sim \pm 3 R_S$  of the equatorial plane. The top of Figure 5 shows that the latitudinal confinement is much less for  $H_2^+$ . Both frames of Figure 5 suggest that the

latitudinal confinement is considerably relaxed near the dayside magnetopause ( $X_{Szs} \sim 17\text{--}20$  in the Figure). The excellent coverage in this region is due to the multiplicity of highly inclined orbits that intersect Titan's orbit, as required for gravity-assisted trajectory changes. The results shown in Figure 5 are very similar to the findings for energetic particles reported by Krimigis et al. [2007] and Sergis et al. [2009].

[31] Both frames of Figure 4 show intriguing spikes near the orbit of Titan. Inspection of the full latitude coverage (not shown) indicates that the enhancements in  $H_2^+/H^+$  appear to be confined to within  $\sim 2^\circ$  of the equatorial plane, while those for  $W^+/H^+$  are less closely confined. It is not clear if any of these enhancements are associated with Titan: there is no expectation that Titan is a significant source of  $W^+$  [e.g., Johnson et al., 2009], and at least one of the episodes of enhanced  $W^+/H^+$  occurred when Cassini was near 11 LT, while Titan was near 16 LT (downstream of Cassini). A more detailed analysis of these enhancements is, however, beyond the scope of the present study.

### 3.3. Scale Heights

[32] To be more quantitative about the latitudinal confinement of the different species, we have computed the scale heights for the density variation perpendicular to the equatorial plane for several different  $L$  ranges. Following Persoon et al. [2006], we express the density of species  $j$  as a function of latitude  $\lambda$  along a given dipole  $L$  shell as,

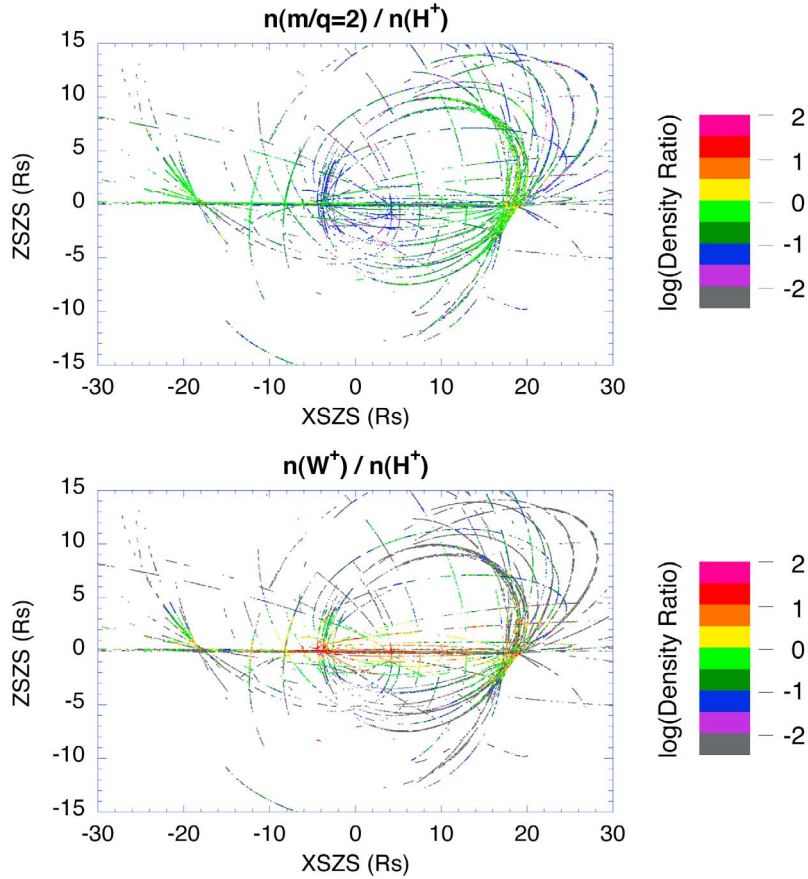
$$n_j = n_{0j} \exp \left[ -L^2 (1 - \cos^6 \lambda) / 3H_j^2 \right]. \quad (1)$$

Figure 6 shows an example of the resulting fits to densities measured between dipole  $L$  values of 6 and 7. For this analysis, we have restricted attention to intervals when the corotation direction was within the CAPS field of view. Converting the exponential fitting parameters  $B_j$  shown in Figure 6 to a scale height by the relationship,

$$H_j^2 = L^2 / 3B_j, \quad (2)$$

we find scale heights for  $H^+$ ,  $H_2^+$ ,  $W^+$ , and total ions in this  $L$  range of  $2.97$ ,  $2.26$ ,  $1.27$ , and  $1.76 R_S$ , respectively. The latter value (for total ions) can be compared to the scale heights derived for the electron density by Persoon et al. [2006], which were  $1.08 R_S$  at  $L = 6$  and  $1.48 R_S$  at  $L = 7$ . The data analyzed by Persoon et al. were primarily from lower latitudes, with  $(1 - \cos^6 \lambda)$  not exceeding 0.25 for the scale-height determinations at  $L = 6$  and  $L = 7$ . If we similarly restrict our analysis to  $(1 - \cos^6 \lambda) < 0.25$ , we find a scale height for the total ions of  $1.20 R_S$  for  $6 < L < 7$ , intermediate between the Persoon et al. values at  $L = 6$  and  $L = 7$ . For this lower range of latitude, the fits for the individual species yield scale heights of  $2.46$ ,  $1.67$ , and  $1.03$  for  $H^+$ ,  $H_2^+$ , and  $W^+$ , respectively.

[33] We can also compare our exponential fits with the latitudinal profiles inferred by Persoon et al. [2009], based on the full field-aligned force equation. Our fits for  $L = 6.5$  (from data between  $L = 6\text{--}7$ ) match the total electron densities versus latitude shown in their Figure 10 for  $L = 6.4 \pm 0.2$  to within  $\sim 25\%$  but do not fall off with latitude as fast as the Persoon et al. solution or their measured densities over



**Figure 5.** Color-coded ratio of densities of ions with (top)  $m/q = 2$  and (bottom)  $W^+$  to  $H^+$  as a function of location in SZS  $X$  and  $Z$ . The heavy ions are much more strongly confined to the equatorial plane by centrifugal forces, but there appears to be some relaxation of the confinement near the dayside magnetopause ( $X \sim 17$ – $20$ ). The relative abundance of ions with  $m/q = 2$  peaks near  $X_{\text{SZS}} \sim 20 R_s$  (see also Figure 4).

the latitude range they cover ( $<20^\circ$ ). This is because our solution is constrained by density values at higher latitudes (up to  $43^\circ$ ) that are well above the densities predicted by the Persoon et al. fits. Note that the scale heights derived from the simple fit to equation (1) are not directly comparable to the scale heights inferred by Persoon et al. [2009] because the latter describe only part of the physics determining the latitudinal dependence of the densities, whereas our values simply describe the full latitudinal dependence itself.

[34] The scale heights derived above can be converted to effective equatorial temperatures  $T_j$  using the relationship [Hill and Michel, 1976],

$$H_j^2 = 2kT_j/3mj\Omega^2, \quad (3)$$

where  $m_j$  is the mass of the  $j$ th species and  $\Omega$  is the co-rotational angular velocity. For strict corotation, equation (3) yields

$$kT_j = 3m_j\Omega^2 H_j^2/2 = 1.56(m_j/m_p)(H_j/R_s)^2. \quad (4)$$

[35] For the scale heights derived for  $(1 - \cos^6 \lambda) < 0.25$ , the corresponding effective equatorial temperatures would

be 9.5, 8.7, and 28.2 eV for  $H^+$ ,  $H_2^+$ , and  $W^+$ , respectively, while those from the scale heights over the full range of  $\lambda$  would be 13.8, 16.0, and 42.9 eV for  $H^+$ ,  $H_2^+$ , and  $W^+$ , respectively. For the subcorotational speeds reported in this region by Wilson et al. [2008], these effective temperatures should be reduced by a factor  $\sim(0.8)^2 = 0.64$ , i.e., (8.8, 10.2, 27.5) for the full range of  $\lambda$  and (6.1, 5.6, 18) if just the low-latitude points are used.

[36] Figure 7a shows the derived scale heights for other  $L$  values, obtained as described above for  $L = 6$ – $7$ , and Figure 7b shows the corresponding effective equatorial temperatures from equation (4), again assuming full corotation. Also shown in Figure 7b, as the heavy curves with no symbols, are the parallel  $H^+$  and  $W^+$  temperatures derived from CAPS low-latitude measurements for  $L < 10$  by Wilson et al. [2008]. Except in the  $L = 6$ – $7$  bin, the water group effective equatorial temperature agrees extremely well with the parallel water group temperature of Wilson et al. With a correction for subcorotation, the effective temperature is higher than the Wilson et al. values at the lowest  $L$  values but does not rise with  $L$  as rapidly as the measured equatorial values, and it is lower than the Wilson et al. values beyond  $L \sim 7$ . A similar situation holds for the effective  $H^+$  temperature shown in Figure 7b: The values are above the

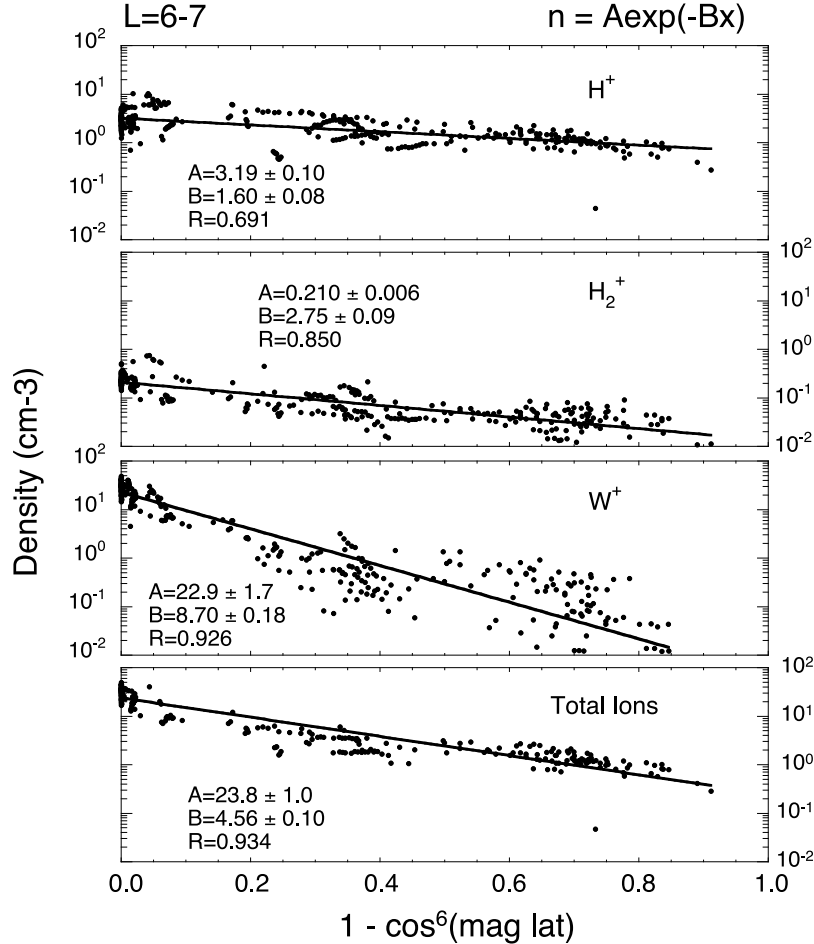


**Figure 6.** Latitude dependence of the density of (from top to bottom),  $H^+$ ,  $H_2^+$ ,  $W^+$ , and total ions in the range  $6 < L < 7$ . The densities are fit to an exponential in  $(1 - \cos^6 \lambda)$ , where  $\lambda$  is the dipole magnetic latitude.

equatorial parallel temperatures derived by Wilson et al. at low  $L$ , but they are nearly equal by  $L \sim 10$  (8.5 if subcorotation is included).

[37] We can also compare these effective temperatures with those inferred for  $H^+$  and  $W^+$  by Persoon et al. [2009], based on their more sophisticated scale height analysis. We find that over the region of overlap ( $L = 6\text{--}10$ ), our inferred  $W^+$  temperatures are  $\sim 3$  times higher than those of Persoon et al. ( $\sim 2$  times if we adjust for subcorotation), but our inferred  $H^+$  temperatures are  $\sim 2\text{--}4$  ( $\sim 3\text{--}6$  if adjusted for subcorotation) times lower than their values (in fact, except for the region  $L \sim 5.3\text{--}7$ , their  $H^+$  temperature actually exceeds their  $W^+$  temperature, which is not in accord with either the measurements reported in our temperature section below or with those reported by other researchers [e.g., Sittler et al., 2005; Wilson et al., 2008]).

[38] In reality, of course, the simple expressions in equations (1)–(4) are not strictly applicable for strongly anisotropic plasmas like those observed in the inner Saturnian magnetosphere. Even the more rigorous analyses of Sittler et al. [2008] and Persoon et al. [2009] do not take into account the fact that each species may have more than one component with different temperatures and anisotropies. A more complete analysis should be pursued that includes all of these effects. This, however, is beyond the scope of

the present survey. In the meantime, the inclusion of the high-latitude points in this study at least allows us to see that the densities do not fall off as rapidly at high latitudes as would be predicted from the lower-latitude measurements of Persoon et al. [2006, 2009], suggesting that the presence of a suprathermal component may be responsible [Moncuquet et al., 2002].

[39] Figure 7c shows the effective equatorial densities inferred from the fits to equation (1) (i.e., the values  $n_{0j}$  in that equation). These densities are  $\sim 3\text{--}10$  times lower than the bulk of the measured values shown in Figure 3a, which again presumably reflects the importance of the temperature anisotropy and mirror force in confining more of the plasma to the equatorial plane. The dipole approximation for the magnetic field that led to equation (1) [Persoon et al., 2006] also becomes increasingly inappropriate beyond  $L \sim 10$  and the correlation coefficients shown in Figure 7d confirm that the fit to  $(1 - \cos^6 \lambda)$  becomes increasingly poor with increasing radial distance. A more rigorous analysis of the vertical distribution of the plasma in the middle magnetosphere is clearly called for in future work.

### 3.4. Temperatures

[40] Figure 8 shows occurrence distributions of the calculated temperatures corresponding to the densities shown

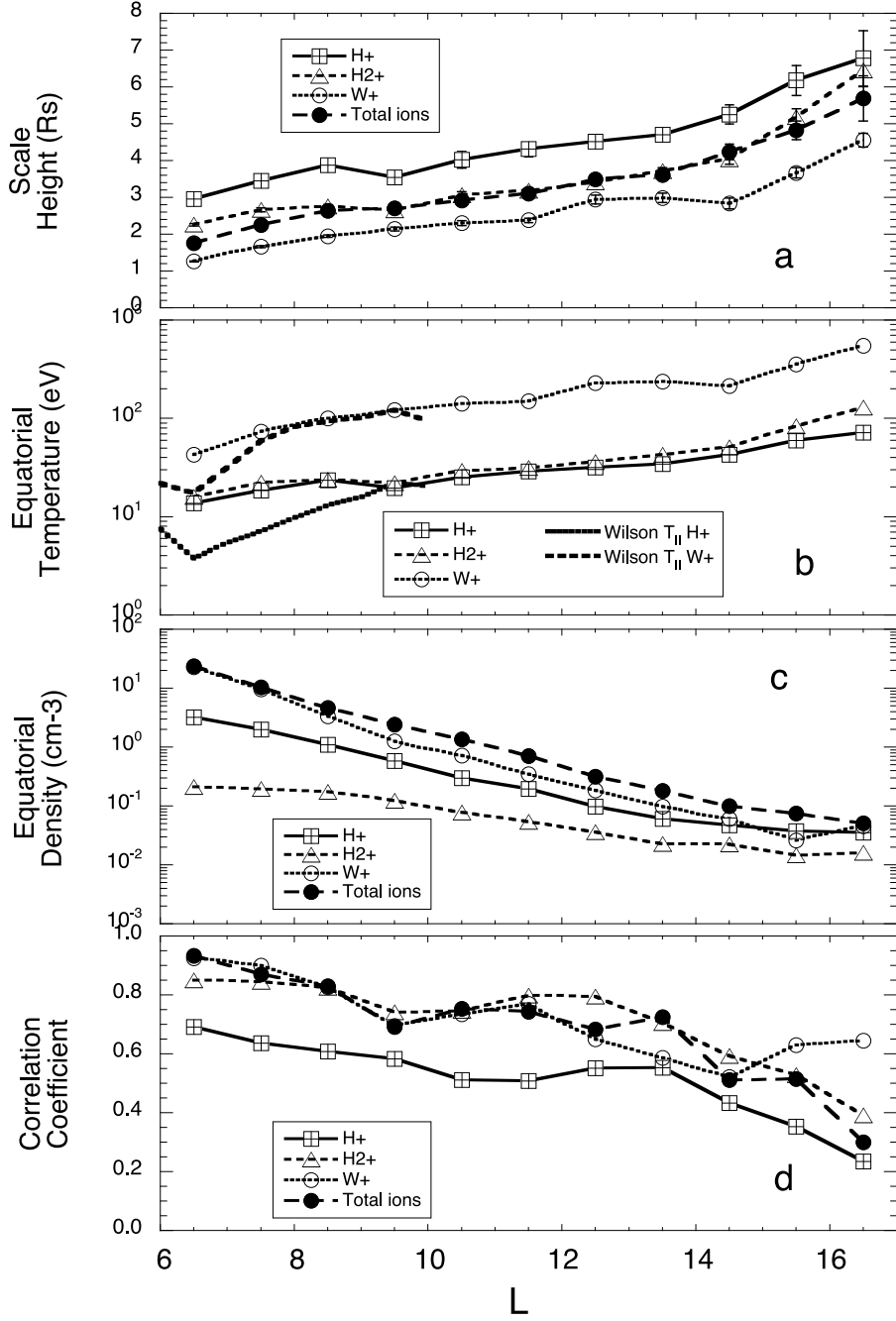


**Figure 7.** (a) Scale heights, (b) effective equatorial temperatures, (c) equatorial densities, and (d) correlation coefficients obtained from linear fitting of measured densities to  $(1 - \cos^6 \lambda)$  for the full range of available  $\lambda$  in various dipole  $L$  ranges.  $\lambda$  is the dipole magnetic latitude, and only data obtained when the corotation direction was within the CAPS FOV are used for the fits. In Figure 7b, the heavy lines without symbols show the values of  $T_{\parallel H}$  and  $T_{\parallel W}$  determined by Wilson et al. [2008].

in Figure 3c (i.e., those points where the strict corotation direction lay within the CAPS FOV and the spacecraft latitude was within  $\pm 5^\circ$  of the equatorial plane). The solid circles indicate the median temperatures over  $1-R_S$  ranges of  $L$ , plotted at the center  $L$  of each range. The data show that all three species have a rather sharp increase in temperature with  $L$  inside  $L \sim 10$ , and beyond that, the temperatures are fairly flat.

[41] The heavy solid curves at low  $L$  in the  $H^+$  and  $W^+$  frames in Figure 8 are derived from the binned values reported in Table 2 of Wilson et al. [2008]. In order to compare with the temperatures obtained from the numerical moments, we have computed weighted averages of the Wilson et al. values, i.e.,  $T_{\text{Wilson}} = (2T_{\perp, \text{Wilson}} + T_{\parallel, \text{Wilson}})/3$ . The Wilson et al. temperatures closely follow the medians for the  $W^+$  temperatures, but only skirt the lower edge of the

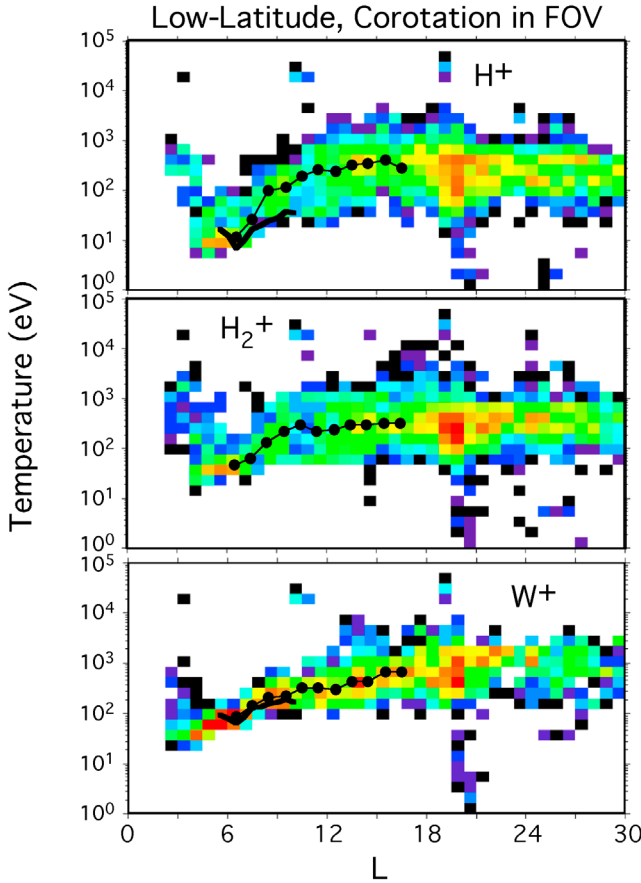


**Figure 8.** Occurrence distribution of the derived temperatures of the three components as a function of  $L$ . Only low-latitude (within  $\pm 5^\circ$  of the equatorial plane) samples with the strict corotation direction within the CAPS field of view are included. The large black dots are the median values for the data segmented into  $1 R_S$  bins, plotted at the center of each bin. The heavy solid lines at low  $L$  are the average ion temperatures for  $H^+$  and  $W^+$  from Table 2 of Wilson et al. [2008].

distribution of  $H^+$  temperatures obtained from the numerical moments. When the data are restricted to only the few intervals included in the Wilson et al. study (not shown), we find that the match to  $T_{W^+}$  is excellent, but the substantial mismatch with  $T_{H^+}$  remains. This is potentially attributable to several possible causes:

[42] 1. The Wilson et al. temperatures were derived from bi-Maxwellian fits to the peaks of the distribution, and the presence of a higher-energy population would not affect them, whereas it would contribute to elevating the numerically determined values. This is particularly a problem for the  $H^+$  because time-of-flight data (not shown) indicate that the hot injected ions [e.g., Hill et al., 2005] are predominantly composed of light ions.

[43] 2. If the flow velocities derived for a given species are not correct, the mismatch will appear as thermal energy (see Appendix B), also leading to an overestimate of the temperature. This also is likely to be more of a problem for  $H^+$  than  $W^+$  because (as discussed below) the velocity

determinations appear to be less reliable for the light ions than for  $W^+$ .

[44] 3. Neither the production numerical moments nor the forward-modeling code used by Wilson et al. properly treat the spacecraft potential, which is typically several volts negative in the inner magnetosphere. The numerical moments calculation assumes the potential is  $-3$  V, while the forward modeling assumed 0 V. It is not clear how this could account for the difference in the derived  $H^+$  temperatures, but again the impact on the  $H^+$  moments would be greater than on the  $W^+$  values.

[45] As noted previously for electrons [Rymer et al., 2007], the  $L$  dependence of the ion temperatures shown in Figure 8 is not consistent with adiabatic transport, either from a source deep inside the magnetosphere or from one at the magnetopause or within the outer magnetosphere. On the other hand, the increase in temperature with radial distance is what one would expect for thermal plasma originating from ion pickup in a nearly corotating flow. Figure 9 shows that the median temperatures of all three species are largely bracketed between the gyrokinetic energies that would be gained by a newly ionized hydrogen ion and a newly ionized water group ion picked up locally at full corotation (thin solid curves). The heavy solid curves that extend only to  $L = 10$  show the local pickup gyrokinetic energies for the same three species for the bulk flow velocities derived by Wilson et al. [2008] for the inner magnetosphere. The same qualitative limits apply, suggesting that it is plausible that local ion pickup is the dominant contribution to the temperature of the ions, with some subsequent redistribution of energy, presumably through collisions or wave-particle interactions. The fact that the median temperatures for the three species tend to cluster together is perhaps additional evidence for collisional sharing of thermal energy.

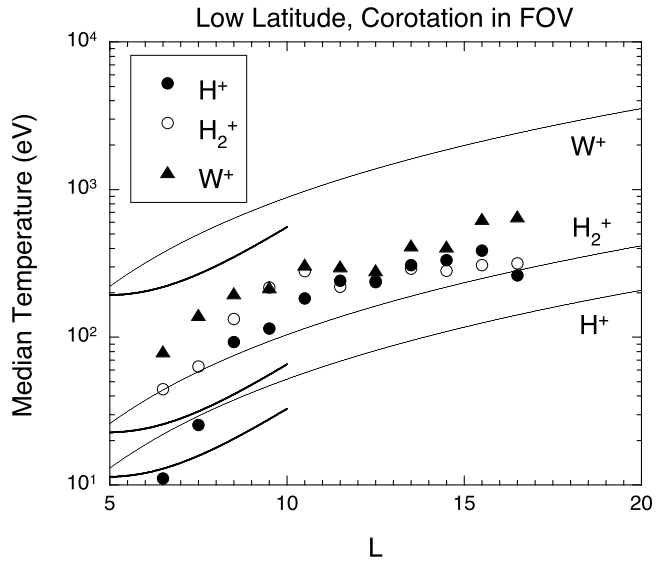


**Figure 9.** Median temperatures of the three ion species, compared with the pickup gyrokinetic energy for full corotation (thin solid lines) and the bulk flow velocity derived by [Wilson et al., 2008] (heavy solid lines, plotted only over the radial range addressed by Wilson et al.).

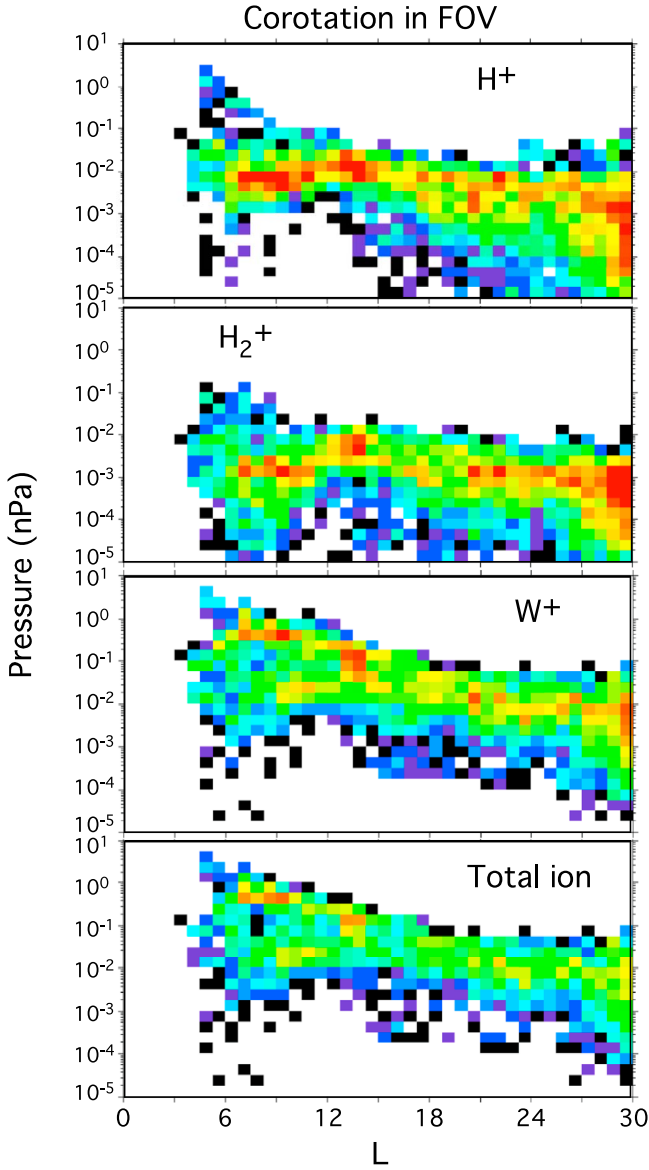


**Figure 10.** Occurrence distribution of derived pressures of the three components and their sum as a function of  $L$ . These pressures represent only the contribution from the CAPS energy range, i.e., below  $\sim 45$  keV. Only points with the strict corotation direction within the CAPS FOV are included.

### 3.5. Pressures

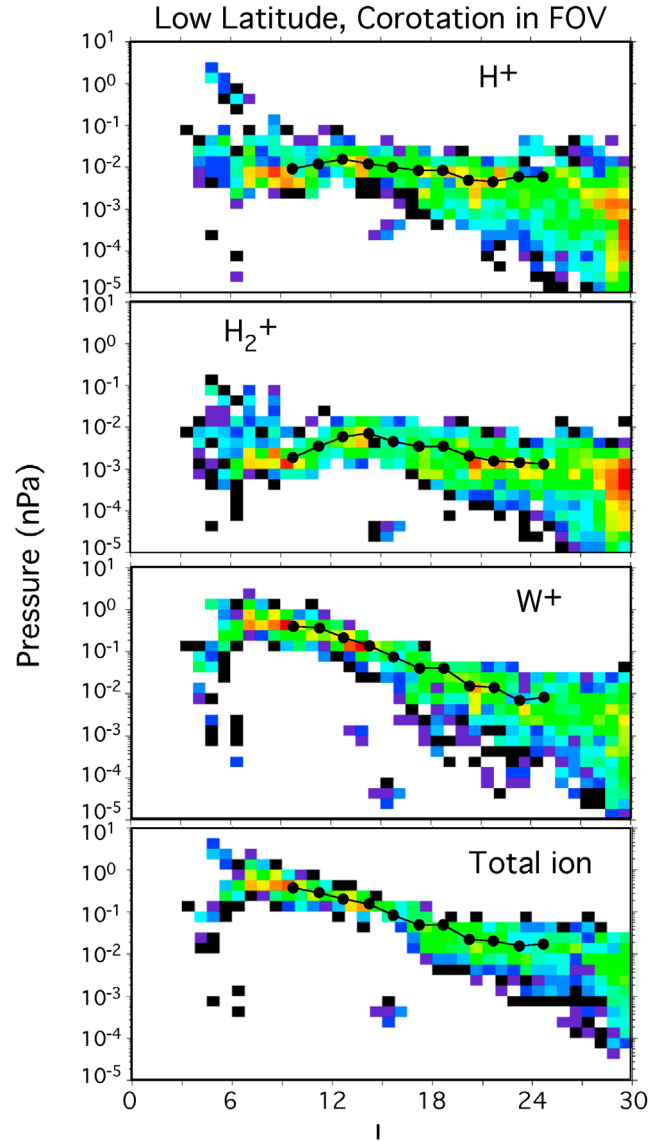
[46] Figure 10 shows the calculated partial pressures in the CAPS energy range for measurements where the corotation direction was in the CAPS field of view, but with all latitudes included. In general,  $W^+$  dominates the ion pressure in this energy range throughout the magnetosphere. The low values in  $W^+$  pressures over the full  $L$  range are primarily attributable to off-equatorial measurements. We illustrate this in Figure 11, which shows only the points that were taken within  $5^\circ$  of the equatorial plane. Comparison of Figures 10 and 11 confirms that the maximum pressures are observed near the equator. The heavy solid dots in Figure 11 show the means in  $1-R_S$   $L$  bins of these low-latitude measurements.

Figure 12 shows just the low-latitude means for all three species, plus the total ions. Near the equator the total ion pressure in the CAPS energy range is clearly dominated by the  $W^+$  ions inside of  $L = 15$ , but the  $H^+$  pressure is comparable to the  $W^+$  pressure beyond that distance.

[47] The dashed line in Figure 12 is a power law fit to the mean binned, low-latitude, total ion pressures. The total ion pressure below 45 keV varies approximately with  $L$  as

$$P_{\text{ion}<45\text{keV}}(\text{nPa}) = 550L^{-3.77}. \quad (5)$$

When this expression is compared with the energetic particle pressures reported by *Sergis et al.* [2009], we find that the total ion pressures in the CAPS energy range (1 eV–45 keV) exceed those in the MIMI range (3–4000 keV) for



**Figure 11.** Same as in Figure 10, with the additional constraint that only points from within  $\pm 5^\circ$  of the equatorial plane are included. Large solid dots show the mean values of the pressures in  $1-R_S$  bins in  $L$ , plotted at the center  $L$  of each bin.

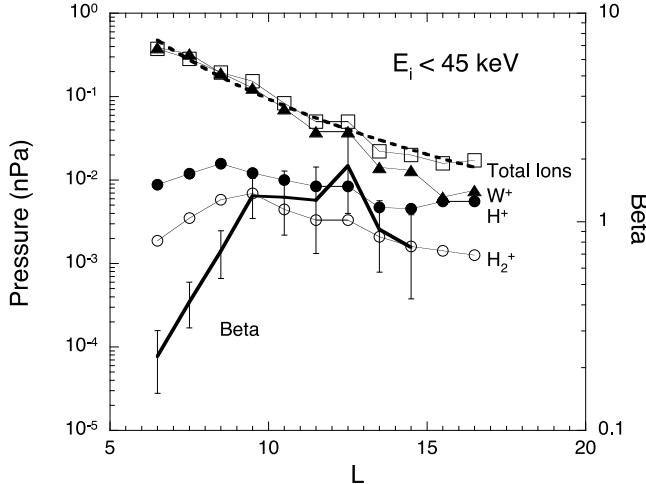


**Figure 12.** Mean values of the pressures (for energies below 45 keV) of the three species and their sum, plotted as a function of  $L$  for only low-latitude points with corotation within the field of view. Except beyond  $L \sim 15$ , the  $W^+$  pressure dominates over the contributions from the lighter ions. The dashed line is a power law fit to the total ion pressure in this energy range, given as  $P_{\text{ion}} (\text{nPa}) = 550 L^{-3.77}$ . Also shown is the contribution to the plasma beta from this energy range, using observed equatorial magnetic field values as presented by Sergis et al. [2010]. The error bars are based on the range of observed equatorial field values in Figure 1b of Sergis et al.

$H^+$  and 9–236 keV for  $O^+$ ) for  $L$  values inside of  $\sim 11$ . Beyond that distance, the pressures in the two (overlapping) energy ranges are comparable. The implication is that inside of  $L \sim 11$ , the particle pressure is dominated by the ion populations below a few keV, while beyond that distance the contributions above 45 keV become more important and at times dominant. Similar conclusions are reached by Sergis et al. [2010], who have done a more comprehensive analysis of the various contributions to the total pressure, as well as a comparison of the different contributions to the ring current (pressure gradient versus inertial currents).

[48] Also shown in Figure 12, as the heavy solid line, is the plasma beta attributable to ions in the CAPS energy range, where we have used the observed values of the equatorial magnetic field pressure presented by Sergis et al. [2010] in their Figure 1b. The error bars represent the range of magnetic pressures observed at each  $L$  value (estimated from Sergis et al. for the same set of center  $L$  values for which we have computed the particle pressure). The presence of the ring current in Saturn's middle magnetosphere reduces the equatorial magnetic field strength compared to the dipole value [e.g., Bunce et al., 2007, and references therein], so the contribution to beta from this energy range is higher than it would be for a dipole field (except for the last point at  $L = 14.5$ ). From Figure 12, the contribution to beta from this energy range exceeds 1 between  $L \sim 9$  and 13, with a peak of less than 2 at  $L \sim 12.5$ . Sergis et al. [2010] have performed a comprehensive study of the total pressure in the magnetosphere, including electrons and higher-energy particles, as well as actual magnetic field measurements, and they find that the total beta exceeds one outside

of  $8 R_S$  and reaches values approaching 20 in the outer magnetosphere.

[49] The radial plasma pressure gradient implied by equation (5) can also be compared with the lobe magnetic field gradient observed by Arridge et al. [2007]. They reported a fit of  $dP_B/dr (\text{N/m}^3) = (1.2 \pm 0.5) \times 10^{-14} r^{-(4.3 \pm 0.1)}$  in the outer magnetosphere (primarily in the tail beyond  $18 R_S$ ). While the range of validity of their radial gradient and that derived here do not overlap by much, extrapolation of their result to  $10 R_S$  yields a magnetic field gradient of  $6.0 \times 10^{-19} \text{ N/m}^3$ , compared with a value of  $5.9 \times 10^{-19} \text{ N/m}^3$  derived from equation (5). A similar extrapolation of our result to  $20 R_S$  yields a plasma pressure gradient of  $2.1 \times 10^{-20} \text{ N/m}^3$ , compared to a magnetic pressure gradient of  $3.0 \times 10^{-20} \text{ N/m}^3$ . As mentioned above, inclusion of the energetic particle pressure (above 45 keV) should increase the particle pressure gradient somewhat above what is derived from equation (5). However, the results of Sergis et al. [2010] show that the energetic particle pressure has a near-zero radial gradient near  $L = 10$  and even at  $15 R_S$  may at best double the pressure gradient derived from CAPS alone. The close agreement of the CAPS ion pressure gradient and the Arridge lobe magnetic pressure gradient over this broad range of  $L$  suggests that the Arridge expression may be valid well inward of the range of  $L$  used to derive it.

### 3.6. Velocities

[50] As described above, because CAPS does not normally view the entire  $4\pi$  steradians of solid angle, and because the plasma flow in Saturn's magnetosphere is typically trans-sonic, valid measurements of the plasma moments can only be obtained when the look direction of the CAPS IMS includes the bulk flow. In our examination of several of the parameters discussed above, we restricted our attention to measurements that were obtained when the strict corotation direction was within the CAPS field of view. To explore the spatial variations of the plasma flow velocity itself, however, this is clearly not an appropriate constraint. Rather, we need a different way to try to restrict the observations to times when CAPS was most likely viewing the bulk of the flowing distribution. The careful analysis of Wilson et al. [2008] imposed the severe criterion that the peak of the counts be well resolved in the field of view, i.e., that the peak not lie at any extremes of anode or actuation angle. In the present work, we adopt a somewhat less restrictive condition: We assume that the higher-density measurements are likely the ones where the instrument captured the main part of the distribution, and we simply accept all the measurements where the density exceeds the mean value for the local  $L$  value, as given by the exponential fits listed in Table 1. In addition, we restrict attention to the low-latitude ( $< 5^\circ$ ) locations where these fits are obtained, and we impose the other standard requirements (the actuator was actuating, the spacecraft was not rolling, and the iteration in the moments calculation was successful).

[51] Figure 13a shows the resulting set of  $W^+$  flow velocities (thinned by a factor of 3 to improve visibility of the vectors), projected to the Szs equatorial plane. The start point of each vector is shown as a small cross.

[52] The global circulation pattern for Saturn's magnetosphere is readily apparent from Figure 13a: Inside of  $\sim 20 R_S$  at all local times, and on the dayside essentially all the way

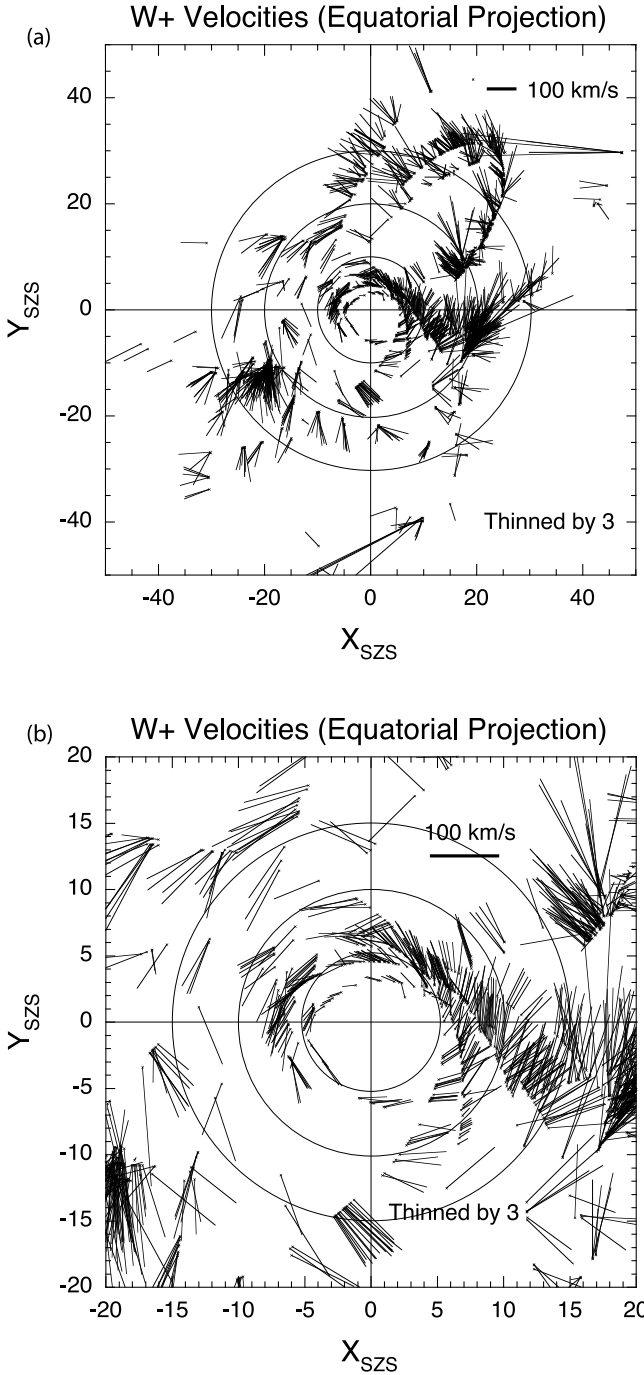


**Figure 13.** (a) Equatorial projections of derived  $W^+$  flow velocities from measurements at latitudes below  $5^\circ$  and with densities above the  $L$ -dependent means listed in Table 1. Crosses show the start point of each vector. Only every third measurement is shown for clarity. (b) Same as in Figure 13a, but only the region inside of  $20 R_S$  is shown.

out to the magnetopause, the flows are dominantly in the corotational direction (providing a posteriori justification for our above restriction to measurements with the corotation direction within the field of view). In the dusk sector, the flows beyond  $20 R_S$  show an alignment with the magneto-

pause, while in the premidnight-to-dawn sector, beyond  $20 R_S$  the flows typically have a tailward and downward direction, as previously reported by McAndrews *et al.* [2009]. There is no evidence in these flows for return circulation from the nightside to the dayside beyond  $20 R_S$ , as discussed more extensively by McAndrews *et al.* However, bearing in mind our selection criterion (namely, above-average density), Figure 13a is best interpreted as showing that the heavily loaded flux tubes containing water group plasma of inner magnetospheric origin are not able to circulate back to the dayside beyond  $\sim 20 R_S$  and are presumably replaced by low-density flux tubes resulting from the down-tail loss (via magnetic reconnection or some other process) of the dense inner magnetospheric plasma.

[53] Figure 13b shows the same data as Figure 13a, for just the region inside  $20 R_S$ . There is the suggestion from a number of the intervals shown in Figure 13b that there is a significant radial (or sunward) component to the flow in the dayside middle magnetosphere. While this may be true, it is more likely that this apparent radial flow is an artifact of the typical viewing that CAPS has on the dayside: Because of the requirements of the optical instruments to observe Saturn and its rings in daylight, the corotation direction is often only barely accessible to the CAPS FOV at the extreme actuation angle. Thus, most of the observed plasma is seen to be coming from the direction of Saturn because that is where the instrument is looking, and as described in Appendix B, our moments algorithm will always return a flow velocity that is within the FOV. We intend to do a more careful analysis of the flows in this region by modifying our analysis to take advantage of the intervals when the spacecraft was rolling, providing more complete velocity space coverage.

[54] Figure 14 shows the  $L$  dependence of the azimuthal flow component ( $V_{\phi}$ ) for all three species, selected according to the low-latitude, higher-than-average-density criteria above. The straight lines in the three frames show the equatorial full-corotation flow speed. Figure 15 shows the same azimuthal components, normalized to the equatorial full-corotation speed. The measured flow speeds for all three species are characteristically below full corotation throughout the entire  $L$  range displayed. The values shown in Figures 14 and 15 are consistent with those reported in the same  $L$  range on the nightside by McAndrews *et al.* They are also consistent with the Voyager 2 values [Richardson, 1998] but are somewhat lower (by  $\sim 20\%-50\%$ ) than those derived from INCA anisotropies by Kane *et al.* [2008].

[55] Figure 16 shows the mean azimuthal flow speeds in the same  $1-R_S$   $L$  bins we have used earlier. The selection criteria are the same as for Figures 13–15. The error bars correspond to the standard deviation for the  $W^+$  means. The error bars for  $H^+$  and  $H_2^+$  are typically larger by  $\sim 20\%-100\%$ . The heavy dashed curve in Figure 16 is the analytical expression given for  $V_\phi$  in Table 3 of Wilson *et al.* [2008]. The heavy solid line is a similar fit to the  $W^+$  velocities from the present study for just the intervals included in the Wilson *et al.* study. Our agreement with the Wilson results is quite good when we compare the same intervals. From Figure 16, however, our typical derived azimuthal velocities are  $\sim 15\%-20\%$  lower than those found for the carefully selected intervals addressed by Wilson *et al.* It is presently unclear whether this is attributable to errors in calculating velocities

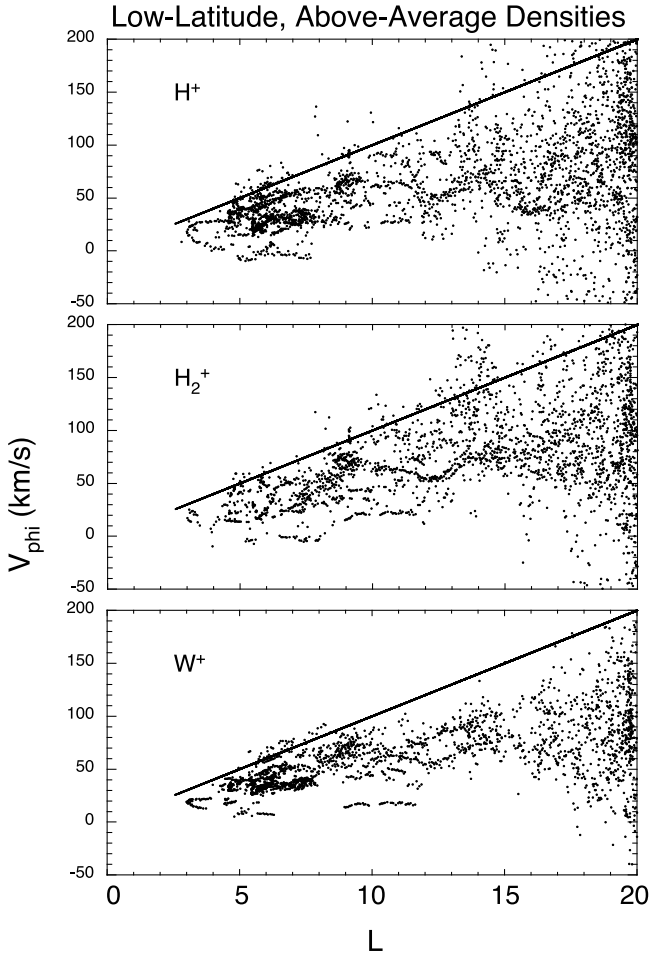


**Figure 14.** Azimuthal flow speeds derived independently from the three different species for measurements obtained at latitudes less than  $5^\circ$  and with densities greater than the means determined from the exponential fits of Table 1. The solid line in each frame shows the equatorial value of full corotation.

when the full distribution is not clearly within the field of view, or whether the flow velocities were actually lower during some of the other intervals we included.

[56] Figure 16 shows that the mean azimuthal flow speeds independently derived from the three species are not in agreement, although physically they must share the same  $E \times B$  flow velocity. The mismatch in the means is certainly within their standard deviations, but it is worthwhile to investigate more carefully the correlation between the flows derived for the three species. The left-hand column of Figure 17 shows the comparison for all the azimuthal velocities included in Figures 13–16, i.e., for points at latitudes below  $5^\circ$ , where the densities exceeded the mean densities given by the exponential fits in Table 1. In the bottom left frame, the correlation is shown for the azimuthal flow velocities derived for  $H^+$  and ' $H_2^+$ ', which certainly includes many points from the magnetosheath and possibly the solar wind; thus, for many of those points the ion with  $m/q = 2$  is  $He^{2+}$ . The frame shows that for the full range of environments (magnetosphere through solar wind), the correlation between the derived azimuthal flow velocities

of  $H^+$  and ions with  $m/q = 2$  is quite good. Over most of the range of values, the agreement is within 30%. However, at low values of the velocity (<50 km/s), such as prevail in the inner magnetosphere (c.f., Figure 14), the two determinations can disagree by a factor of 2 or more.

[57] The top left and center left frames of Figure 17 show that the azimuthal flow velocities derived from the light ions are less well correlated with those from the  $W^+$  ions than with each other. In particular, there is a population of points in both frames in which the derived light-ion flow speed is much greater than that for  $W^+$ . The bulk of these points turn out to be obtained in the magnetosheath or solar wind, where the mean densities derived from Table 1 (and thus our density constraint) do not apply, especially for  $W^+$ . If we restrict our attention to points obtained for  $L < 15$ , we obtain the right-hand set of frames in Figure 17. The anomalous population disappears, and the correlations between the various populations are quite respectable. However, based on examination of individual time series (not shown), we find that the flow velocity determined from the  $W^+$  population typically has less scatter (see also Figure 14) and is to be preferred to that from the other populations if  $W^+$  is present at appreciable levels. In the solar wind and mag-

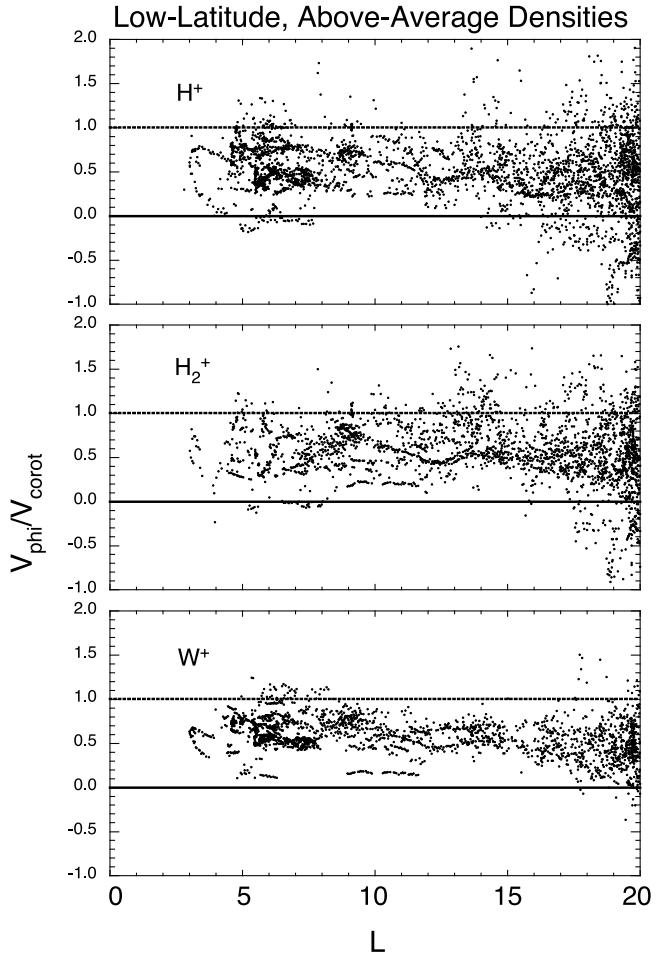


**Figure 15.** Same as in Figure 14, but the flow speeds are normalized to the full-corotation value.

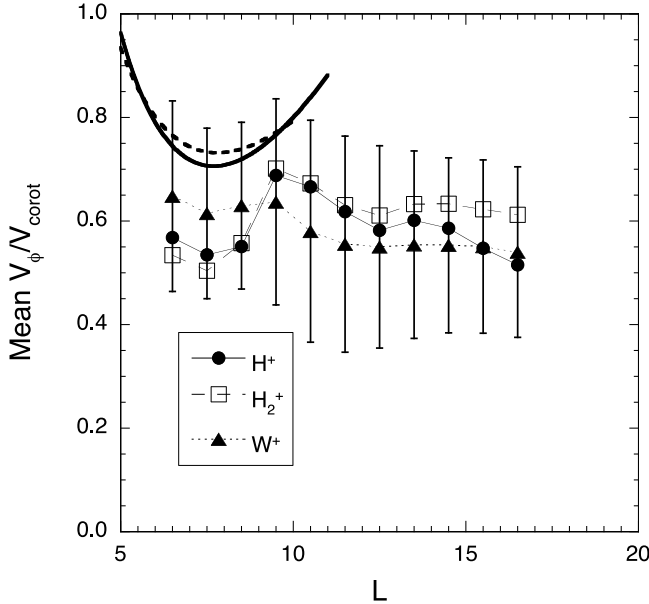


**Figure 16.** Mean values of the normalized flow speeds shown in Figure 15, from  $1-R_S$  bins in  $L$ . The means are plotted at the center  $L$  of the corresponding bins. The error bars show the standard deviations in the means for the  $W^+$  population. The heavy dashed line is the quadratic fit to  $V_\phi$  reported by Wilson *et al.* [2008] for a carefully selected set of inner magnetospheric observations, and the heavy solid line is a similar fit to the numerical moments obtained in the same set of intervals.

netosheath, of course, the determination from the light ions is obviously to be preferred.

#### 4. Summary

[58] We have presented a survey of plasma parameters derived from numerical integration of 4.5 years of CAPS/IMS Singles data (26 October 2004 to 31 March 2009), partitioned into three species ( $H^+$ ,  $H_2^+$  or  $He^{2+}$ ,  $W^+$ ) based on concurrent time-of-flight measurements. When properly filtered according to specified criteria, the observations lead to the following findings:

[59] 1. The densities of the three components are highly variable but on the whole are organized by  $L$  and latitude. Upper limits of observed densities follow an  $r^{-4}$  dependence throughout much of the magnetosphere out to the magnetopause, but the mean densities at low latitudes can be well described by both an exponential in  $L$  and a power law in  $L$  (Table 1).

[60] 2. The density of ions with  $m/q = 2$  tracks the  $H^+$  density fairly well throughout the magnetosphere, with ratios of about several percent in both the inner magnetosphere (where the ions with  $m/q = 2$  are probably  $H_2^+$ ) and the magnetosheath/solar wind (where the ions with  $m/q = 2$  are certainly  $He^{2+}$ ). In the outer magnetosphere the ratio rises to several tens of percent, so that ions with  $m/q = 2$  constitute a significant contribution to the total density, well exceeding what would be expected from solar wind plasma. The ratio of  $H_2^+/H^+$  peaks near Titan's orbit, suggesting that Titan is an important source for  $H_2^+$  in the

outer magnetosphere, as predicted theoretically [Cui *et al.*, 2008].

[61] 3. The density of  $W^+$  is less well correlated with  $H^+$ , primarily because of stronger equatorial confinement of heavy ions. Even in the inner magnetosphere,  $W^+$  dominates over  $H^+$  only within  $\sim 3 R_S$  of the equator.

[62] 4. For a latitudinal variation of density of the form  $n_j = n_{0j} \exp[-L^2(1 - \cos^6\lambda)/3H_j^2]$  [cf., Persoon *et al.*, 2006], the derived scale heights  $H_j$  for  $j = H^+$ ,  $H_2^+$ , and  $W^+$  vary from 3, 2.3, and 1.3, respectively, at  $L = 6-7$  to 6.8, 6.5, and 4.6, respectively, at  $L = 16-17$ . The scale height for the total ion density is quite similar to that of  $H_2^+$  over the full radial range. The corresponding equivalent equatorial temperatures are comparable to the parallel equatorial temperatures determined by Wilson *et al.* [2008]. A more rigorous analysis of the latitudinal variation of plasma properties in the middle magnetosphere will need to take into account the significant anisotropies present in the equatorial distribution functions, as well as the presence of multiple populations and the nondipolar nature of the magnetic field.

[63] 5. The calculated temperatures have a rather sharp increase with  $L$  inside of  $L \sim 10$  and beyond that are fairly flat. This  $L$  dependence is not consistent with adiabatic transport but is in fair agreement with the expectations for plasma originating from ion pickup. The median temperatures of all three species are bounded by the gyration energies that would be gained by a newly ionized  $H^+$  ion and a newly ionized  $W^+$  ion picked up locally. Thus, it is plausible that local ion pickup is the dominant contribution to the temperature of the ions, with some subsequent redistribution of energy, presumably through collisions or wave-particle interactions.

[64] 6.  $W^+$  dominates the ion pressure in the CAPS energy range, except at higher latitudes and beyond  $L \sim 15$ . The equatorial total ion pressure for particles below 45 keV varies as  $L^{-3.77}$ . Comparison with pressures derived from MIMI data [Sergis *et al.*, 2009] suggest that inside of  $L \sim 11$ , the particle pressure is dominated by ions with energies below a few keV, while beyond that distance the contributions above 45 keV become increasingly important and at times dominant, in agreement with the conclusions of Sergis *et al.* [2010]. The plasma beta attributable to ions in the CAPS energy range varies from a few tenths in the inner magnetosphere to a peak of less than  $\sim 2$  near  $L \sim 12.5$ , declining again beyond that.

[65] 7. The derived flow velocities reveal the global circulation pattern of relatively dense populations within Saturn's magnetosphere: Inside of  $\sim 20 R_S$  at all local times and on the dayside essentially all the way out to the magnetopause, the flows are dominantly in the corotational direction. In the dusk sector, the flows beyond  $\sim 20 R_S$  are roughly aligned with the magnetopause, while in the pre-midnight-to-dawn sector, the flows typically have a tailward and downward direction, with no evidence for return circulation from the nightside to the dayside beyond  $20 R_S$ , as previously reported by McAndrews *et al.* [2009]. The magnetic flux carried away by these denser flows is presumably returned to the dayside within low-density flux tubes resulting from the down-tail loss (via magnetic reconnection or some other process) of the dense inner magnetospheric plasma.

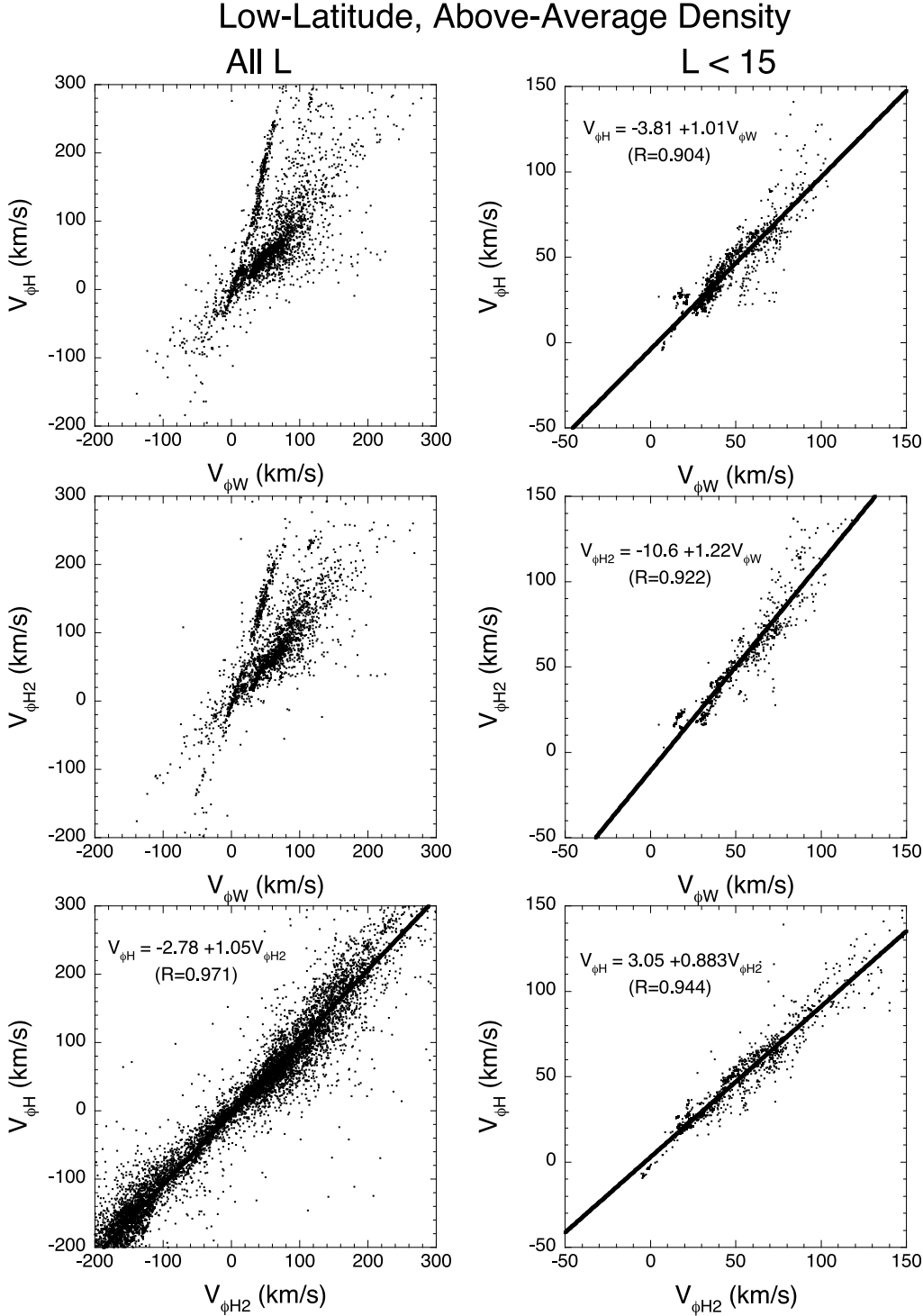


**Figure 17.** Comparison of azimuthal flow speeds derived independently from the three different species for measurements obtained at latitudes less than  $5^\circ$  and with densities greater than the means determined from the exponential fits of Table 1. The left-hand column includes all  $L$  values, while the right-hand column includes only points for  $L < 15$ .

[66] 8. The measured azimuthal flow speeds for all three species are characteristically below full corotation over the entire  $L$  range examined, varying from  $\sim 50\%$  to  $\sim 70\%$  on average. Within the magnetosphere, azimuthal flow speeds derived independently from the three species are in generally good agreement with each other, but the values from

$W^+$  typically have less scatter and are to be preferred to those from the other populations if  $W^+$  is present at significant levels.

[67] The ion plasma measurements presented in this study are generally in good agreement with various parameters derived or inferred by previous authors. While the future

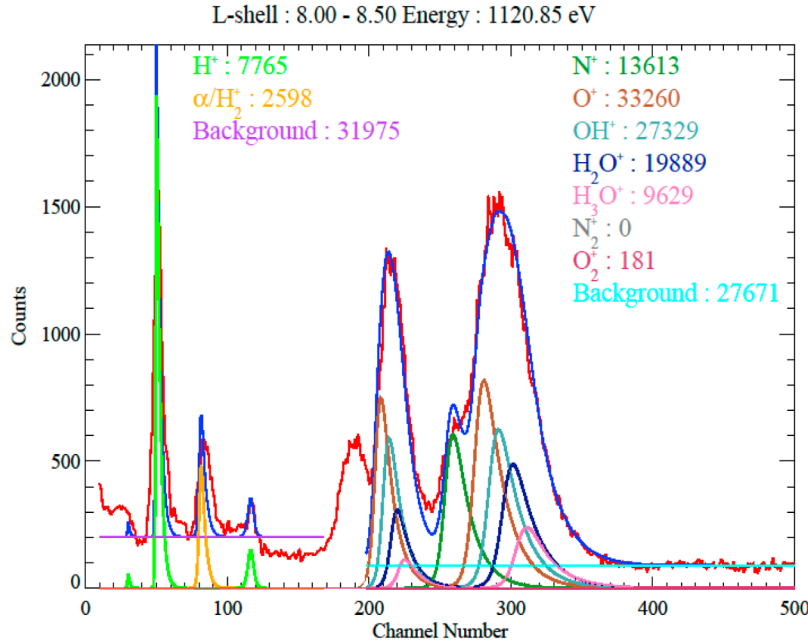


**Figure A1.** Counts in the ST detector as a function of TOF for energy 1120 eV, summed from  $L = 8.0 - 8.5$ . After time-of-flight spectra are binned, we determine the contribution of individual masses to each spectrum by fitting model functions determined from calibration data. The plot shows the relative amounts of different ion components (various colors) that comprise the peaks on the TOF spectrogram data (red line). The sum of all model constituents is given by the blue line. Note there are two  $\text{W}^+$  peaks. Before an ion's TOF is measured, the ion passes through a thin carbon foil, knocking off electrons, which serve to generate a start pulse. The right peak is due to oxygen from  $\text{W}^+$  that exits the foil as a neutral; the left is from oxygen that exits the foil as a negative ion. Fitting is best accomplished by dividing the time-of-flight interval into two sections characterized by distinct background levels. The first includes  $\text{H}^+$  and light atomic mass species and the second includes  $\text{W}^+$  and heavier atomic mass species. The gap between the two fits contains a peak due to TOF starts from postfoil  $\text{H}^-$  ions rather than electrons. At this energy,  $\text{O}_2^+$  would be expected at TOF channels 440–450, but for this sample of data there are too few counts in this range to be distinguishable from background.

development of an improved analysis algorithm will provide a refined and expanded set of moments, the parameters described above provide a valuable global picture of Saturn's magnetospheric plasma environment.

## Appendix A: Partition of SNG Counts Into Select Species

[68] This appendix describes the method by which the TOF spectra are analyzed to determine the relative abundances of  $\text{H}^+$ ,  $\text{H}_2^+/\text{He}^{2+}$ , and  $\text{W}^+$  (comprising  $\text{O}^+$ ,  $\text{OH}^+$ ,  $\text{H}_2\text{O}^+$ , and  $\text{H}_3\text{O}^+$ ). As mentioned earlier, mass analysis occurs within a time-of-flight analyzer that follows a thin carbon foil. Ions exiting the electrostatic analyzer are accelerated and pass through the carbon foil, where they exit either as neutrals or ions. If the incident ion is a molecule, it is also disassociated into its constituent atoms by the foil. The IMS mass analyzer is actually composed of two sensors: a high-resolution sensor (resolution  $M/\Delta M \sim 60$ ) that takes advantage of the linearly-varying electric field (LEF) within the TOF analyzer to detect time-focused positive ions and a medium-resolution sensor ( $M/\Delta M \sim 8$ ) that measures the TOF of species that exit the foil as neutrals, negative ions, or positive ions  $> 16$  keV. Although of significantly lower mass resolution, this so-called “straight-through” (ST) sensor

detects species with  $\sim 20$  times the efficiency of the LEF sensor. In addition, identification of the molecular parent ion is possible with the ST sensor, but not as easily with the LEF sensor. For these reasons, the species partitioning is performed on TOF spectra collected by the ST sensor.

[69] To identify particular species within a TOF spectrum, a Levenberg-Marquardt least squares minimization algorithm is used, whereby model TOF peaks representing individual candidate species are fit to the raw data. For the core fitting routine, we make use of a publicly available IDL source code called MPFIT, available from NASA Goddard Space Flight Center [Markwardt, 2008] (MPFIT is available at <http://purl.com/net/mpfit>).

[70] TOF spectra are collected at all 64 IMS energy steps, but due to telemetry limitations, these are collapsed pairwise into 32 spectra. Each resulting spectrum is separately fit to determine the number of counts associated with the various species. Figure A1 shows a typical ST TOF spectrum, for 1120 eV ions collected in an  $L$  shell interval between 8 and 8.5. Overlaid on the raw counts are the corresponding peak fits. The model peaks are derived from calibration of the flight unit and account for the main peaks due to species exiting the foil as neutrals, as well as certain satellite peaks. In the case of oxygen-bearing species, we account for the large satellite peak (channels 200–240) due

to atoms exiting the foil as negative oxygen ions. In the case of hydrogen, there are two satellite peaks: hydrogen exiting the foil as a negative ion (channel 30) and hydrogen exiting as a proton, striking the LEF sensor, and emitting secondary electrons that create an “echo” on the ST sensor (channels 110–120). In addition, two flat “backgrounds” are fit to the spectrum. The first roughly accounts for the rather ragged “ghost structure” due to scattering within the instrument between channels 10 and 170. The effect on the TOF spectrum due to the ghost structure has been successfully modeled, but for efficiency, we simply fit this to a flat line. The second flat line fit is for counts in channels above 200. Between channels 170 and 200, the ghost structure transitions to a much flatter spectrum and can be accurately fit by a flat line. The unfitted peak present in this gap is due to TOF starts from postfoil H<sup>−</sup> ions rather than electrons.

[71] Once the various peaks relevant to each desired species have been fit, the fitted peaks are integrated and the resulting counts are attributed to the appropriate species. Although we determine separately the number of counts associated with individual water group species, for the present study, the O<sup>+</sup>, OH<sup>+</sup>, H<sub>2</sub>O<sup>+</sup> and H<sub>3</sub>O<sup>+</sup> counts are summed to determine the total W<sup>+</sup> content. The N<sup>+</sup> counts are also determined, but are not included in the W<sup>+</sup> sum. Each species’ summed TOF counts are then divided by the appropriate energy- and species-dependent stop efficiency to identify the relative contribution to the start-only signals of SNG. These efficiency-corrected sums are then further summed over all species to obtain the total efficiency-corrected TOF counts recorded at that energy level. Each efficiency-corrected TOF species sum is finally divided by the total efficiency-corrected TOF sum to identify the fraction of SNG counts to attribute to each species.

## Appendix B: Numerical Computation of Plasma Moments

[72] A full description of the algorithm and analysis routine used to compute the numerical plasma moments from CAPS IMS data is contained in the work of *Thomsen and Delapp* [2005], available from the authors or online at [http://nis-www.lanl.gov/nis-projects/caps/Moments\\_Computation.pdf](http://nis-www.lanl.gov/nis-projects/caps/Moments_Computation.pdf). This appendix presents a highly abbreviated form of that description.

[73] For each target species, the moments computed from CAPS measurements are the density, vector flow velocity, and temperature tensor, defined respectively as

$$n = \int_{\text{all } \mathbf{v}} f(\mathbf{v}) d^3 \mathbf{v}, \quad (\text{B1a})$$

$$\mathbf{V} = ({}^1/n) \int_{\text{all } \mathbf{v}} \mathbf{v} f(\mathbf{v}) d^3 \mathbf{v}, \quad (\text{B1b})$$

$$\underline{\mathbf{T}} = ({}^m/n) \int_{\text{all } \mathbf{v}} (\mathbf{v} - \mathbf{V})(\mathbf{v} - \mathbf{V}) f(\mathbf{v}) d^3 \mathbf{v}. \quad (\text{B1c})$$

[74] These moments are all integrals of the form,

$$M = \int_{\text{all } \mathbf{v}} g(\mathbf{v}) f(\mathbf{v}) d^3 \mathbf{v}, \quad (\text{B2})$$

where  $f(\mathbf{v})$  is the velocity distribution function and the velocity functions  $g(\mathbf{v})$  are related to the desired moments. The integral in equation (B2) is to be taken over the entire volume of velocity space, which is composed of the part that CAPS views (obs) and the part CAPS does not view (unobs),

$$M = \int_{\text{obs}} g(\mathbf{v}) f(\mathbf{v}) d^3 \mathbf{v} + \int_{\text{unobs}} g(\mathbf{v}) f(\mathbf{v}) d^3 \mathbf{v}. \quad (\text{B3})$$

[75] The production algorithm uses known symmetries of charged-particle distributions to “fill in” unobserved portions of velocity space. In particular, we assume that the distribution is mirror symmetric about the bulk flow velocity  $\mathbf{V}$ , i.e.,

$$f(2\mathbf{V} - \mathbf{v}) = f(\mathbf{v}). \quad (\text{B4})$$

[76] Under this assumption, the observed volume of velocity space can be separated into a “symmetric” portion (sym), containing those observation points whose mirrored (about  $\mathbf{V}$ ) points are also contained in the observed volume of velocity space, and an “unbalanced” portion (unbal), containing observed measurement points whose mirrored values do not lie within the observed space. Similarly, the unobserved portion of velocity space also consists of two parts: (1) the mirror of the unbalanced observed portion (mir unbal) and (2) a remainder. With the assumption of mirror symmetry, equation (B4), the integral over mir unbal can be related to the integral over unbal,

$$\int_{\text{mir unbal}} g(\mathbf{v}') f(\mathbf{v}') d^3 \mathbf{v}' = \int_{\text{unbal}} g(2\mathbf{V} - \mathbf{v}) f(\mathbf{v}) d^3 \mathbf{v}. \quad (\text{B5})$$

[77] Finally, assuming that the remainder term is negligible compared to the amount of the distribution contained in the sym, unbal, and mir unbal portions of velocity space, equation (B3) becomes

$$M \cong \int_{\text{sym}} g(\mathbf{v}) f(\mathbf{v}) d^3 \mathbf{v} + \int_{\text{unbal}} g(\mathbf{v}) f(\mathbf{v}) d^3 \mathbf{v} \\ + \int_{\text{unbal}} g(2\mathbf{V} - \mathbf{v}) f(\mathbf{v}) d^3 \mathbf{v}. \quad (\text{B6})$$

[78] The key to implementing this approach is clearly the determination of the bulk flow velocity,  $\mathbf{V}$ , which is not known a priori. In practice, we use an iterative approach: The velocity is first estimated from equation (B2) using only the observed portion of velocity space. With this estimated velocity, we separate the observed velocity space into the symmetric and unbalanced parts by examining, for each measurement point  $\mathbf{v}$ , whether its mirrored point (2 $\mathbf{V}$  −  $\mathbf{v}$ ) also lies within the observed velocity space. With this par-

tion, we find the corresponding corrected velocity, and continue this iteration until the derived velocity converges. In practice, we require either that the magnitude of  $\mathbf{V}$  is not changed by more than 1% from the previous value or that a maximum of 15 iterations are completed.

[79] When a stable value of  $\mathbf{V}$  has been obtained, the rest of the moments are computed from equation (B6), with the appropriate  $g(\mathbf{v})$ . For the temperature, the resulting  $3 \times 3$  matrix is diagonalized, yielding the three eigenvalues and their corresponding eigenvectors. The eigenvalue that is most different from the other two is identified as  $T_{\text{para}}$  and the average of the other two as  $T_{\text{perp}}$ . In practice, this process is very susceptible to instrument angular-response effects that are not completely removed in the analysis, so for the purposes of the present survey, we use only the trace of the temperature matrix, which is relatively insensitive to the direction of incidence of the particles.

[80] On the basis of the above theoretical foundation, the integrals of equation (B6) are approximated by a straightforward finite difference scheme that weights each measured value of  $f(\mathbf{v}) = f_{sijk}$  with its corresponding volume of velocity space. Here

$$f_{sijk} = \frac{C_{sijk}}{\tau \varepsilon_{si} G_j E_i^2 \alpha_s}, \quad (\text{B7})$$

where  $C_{sijk}$  is the partitioned SNG counts for species  $s$  measured in detector  $j$  at energy level  $i$  and azimuth  $k$ . The parameters in the denominator are as follows:

$$\begin{aligned} \tau &= \text{IMS accumulation interval} = 0.0625 \text{ s}; \\ \alpha_s &= (2/m_s^2) = 1.835e24 (m_p/m_s)^2 (\text{cm}^4/\text{eV}^2 \text{ s}^4); \\ E_i &= \text{energy of level } i \text{ (eV)}; \\ G_j &= \text{geometric factor of detector } j = 1.5008e-3 \text{ cm}^2 \text{ sr eV/eV}; \\ \text{and} \\ \varepsilon_{si} &= \text{detection efficiency for species } s \text{ at energy } E_i, \\ &= (\text{foil transmission}) (\text{dome grid trans}) (\text{MCP grid trans}) \\ &\quad (\text{start efficiency}), \\ &= (0.66)(0.65)(0.9)(0.69) \text{ for SNG,} = 0.266. \end{aligned}$$

[81] Before the species partition is accomplished (see Appendix A), the SNG count rates are first corrected for the background caused by penetrating energetic particles. For SNG, removal of the background is relatively straightforward, since its contribution to the count rate of the instrument should be independent of the voltage setting on the plates and roughly independent of the azimuth, but the background removal is done separately for each anode as follows: For each A cycle and at each energy level, the counts in each detector are averaged over all the separate azimuths. To improve the statistics, an additional average is done over every three energy levels. If the minimum such three-channel average in detector  $j$  for that A cycle is  $\langle C_j \rangle_{\min}$ , the average background for detector  $j$  is estimated to be

$$\mathbf{B}_j = \langle C_j \rangle_{\min} + \text{sqrt}(\langle C_j \rangle_{\min}). \quad (\text{B8})$$

[82] The  $\text{sqrt}$  term in equation (B8) is added under the assumption that for a Poisson-distributed background, the minimum observed rate, is probably below the average by

something like one standard deviation. The estimated average background  $B_j$  is then subtracted from all of the measured count rate bins for detector  $j$ .

[83] After the background is subtracted, the corrected SNG rates are then partitioned into species using the energy-dependent partition factors described in Appendix A.

[84] There are a number of caveats regarding the moments derived from SNG data as described above:

[85] 1. The species partition method described in Appendix A can be significantly in error if time variations in the spectra and composition occur on a shorter time scale than the interval required to accumulate statistically significant counts in a TOF spectrum.

[86] 2. The derived velocity will by construction lie within the instrument field of view. When the FOV actually encompasses the flow velocity, this is not a problem. But when the flow is not directly into the instrument, the returned values will not be correct.

[87] 3. The method is predicated on the actuation of the instrument back and forth across the distribution. When CAPS is not actuating, the iterative scheme will fail.

[88] 4. Because of the  $1/E^2$  dependence of the distribution function, the computed moments (at least for  $H^+$ ) are very strongly influenced by counts in the lowest energy channels, which are likely random background and difficult to remove completely. Therefore, the code zeroes out the channels below a specified energy value. This cutoff energy is one of the input parameters and for most of our runs is set at  $\sim 9$  eV. A lower value should be used in the innermost part of the magnetosphere, where the real signal descends to low energies.

[89] 5. At very high levels of penetrating background, the rather unsophisticated background subtraction is probably inadequate.

[90] **Acknowledgments.** The authors thank Tom Hill for encouragement and very helpful discussions. We also thank both referees for careful and insightful reviews. Work at Los Alamos was conducted under the auspices of the U. S. Department of Energy, with support from the NASA Cassini program. The Cassini Plasma Spectrometer was supported by JPL contract 1243218 with Southwest Research Institute. The Cassini project is managed by the Jet Propulsion Laboratory for NASA.

[91] Masaki Fujimoto thanks Nick Sergis and another reviewer for their assistance in evaluating this paper.

## References

- Arridge, C. S., C. T. Russell, K. K. Khurana, N. Achilleos, N. André, A. M. Rymer, M. K. Dougherty, and A. J. Coates (2007), Mass of Saturn's magnetodisc: Cassini observations, *Geophys. Res. Lett.*, **34**, L09108, doi:10.1029/2006GL028921.
- Arridge, C. S., H. J. McAndrews, C. M. Jackman, C. Forsyth, and A. P. Walsh, et al. (2009), Plasma electrons in Saturn's magnetotail: Structure, distribution and energisation, *Plan. Sp. Sci.*, **57**, 2032–2047.
- Bunce, E. J., S. W. H. Cowley, I. I. Alexeev, C. S. Arridge, M. K. Dougherty, J. D. Nichols, and C. T. Russell (2007), Cassini observations of the variation of Saturn's ring current parameters with system size, *J. Geophys. Res.*, **112**, A10202, doi:10.1029/2007JA012275.
- Cui, J., R. V. Yelle, and K. Volk (2008), Distribution and escape of molecular hydrogen in Titan's thermosphere and exosphere, *J. Geophys. Res.*, **113**, E10004, doi:10.1029/2007JE003032.
- Frank, L. A., B. G. Burek, K. L. Ackerson, J. H. Wolfe, and J. D. Mihalov (1980), Plasmas in Saturn's magnetosphere, *J. Geophys. Res.*, **85**(A11), 5695–5708, doi:10.1029/JA085iA11p05695.
- Hill, T. W., and F. C. Michel (1976), Heavy ions from the Galilean satellites and centrifugal distortion of the Jovian magnetosphere, *J. Geophys. Res.*, **81**, 4561–4565.
- Hill, T. W., A. M. Rymer, J. L. Burch, F. J. Crary, D. T. Young, M. F. Thomsen, D. Delapp, N. Andre, A. J. Coates, and G. R. Lewis (2005),

- Evidence for rotationally driven plasma transport in Saturn's magnetosphere, *Geophys. Res. Lett.*, 32(14), L14S10, doi:10.1029/2005GL022620.
- Johnson, R. E., O. J. Tucker, M. Michael, E. C. Sittler, H. T. Smith, D. T. Young, and J. H. Waite (2009), Mass loss processes in Titan's upper atmosphere, in *Titan From Cassini-Huygens*, edited by R. H. Brown, J.-P. Lebreton, and J. H. Waite, 373–391, Springer, New York.
- Kane, M., D. G. Mitchell, J. F. Carbary, S. M. Krimigis, and F. J. Crary (2008), Plasma convection in Saturn's outer magnetosphere determined from ions detected by the Cassini INCA experiment, *Geophys. Res. Lett.*, 35, L04102, doi:10.1029/2007GL032342.
- Krimigis, S. M., et al. (2005), Dynamics of Saturn's Magnetosphere from MIMI during Cassini's Orbital Insertion, *Science*, 307, 1273.
- Krimigis, S. M., N. Sergis, D. G. Mitchell, D. C. Hamilton, and N. Krupp (2007), A dynamic, rotating ring current around Saturn, *Nature*, 450, 1050.
- Markwardt, C. B. (2008), "Non-Linear Least Squares Fitting in IDL with MPFIT," in Proc. Astronomical Data Analysis Software and Systems XVIII, Quebec, Canada, *ASP Conf. Ser.*, vol. 411, edited by D. Bohlender, P. Dowler, and D. Durand, pp. 251–254, Astron. Soc. Pac., San Francisco, ISBN: 978-1-58381-702-5.
- McAndrews, H. J., et al. (2009), Plasma in Saturn's nightside magnetosphere and the implications for global circulation, *Planet. Space Sci.*, doi:10.1016/j.pss.2009.03.003.
- Moncuquet, M., F. Bagenal, and N. Meyer-Vernet (2002), Latitudinal structure of outer Io plasma torus, *J. Geophys. Res.*, 107(A9), 1260, doi:10.1029/2001JA900124.
- Morooka, M. W., R. Modolo, J. E. Wahlund, M. Andre, and A. I. Eriksson, et al. (2009), The electron density of Saturn's magnetosphere, *Ann. Geophys.*, 27, 2971–2991.
- Persoon, A. M., D. A. Gurnett, W. S. Kurth, and J. B. Groene (2006), A simple scale height model of the electron density in Saturn's plasma disk, *Geophys. Res. Lett.*, 33, L18106, doi:10.1029/2006GL027090.
- Persoon, A. M., D. A. Gurnett, O. Santolik, W. S. Kurth, and J. B. Falden (2009), A diffusive equilibrium model for the plasma density in Saturn's magnetosphere, *J. Geophys. Res.*, 114, A04211, doi:10.1029/2008JA013912.
- Richardson, J. D. (1998), Thermal plasma and neutral gas in Saturn's magnetosphere, *Rev. Geophys.*, 36(4), 501–524, doi:10.1029/98RG01691.
- Richardson, J. D., A. Eviatar, and G. L. Siscoe (1986), Satellite tori at Saturn, *J. Geophys. Res.*, 91(A8), 8749, doi:10.1029/JA091iA08p08749.
- Rymer, A. M., B. H. Mauk, T. W. Hill, C. Paranicas, and N. Andre, et al. (2007), Electron sources in Saturn's magnetosphere, *J. Geophys. Res.*, 112, A02201, doi:10.1029/2006JA012017.
- Schippers, P., M. Blanc, N. Andre, I. Dandouras, and G. R. Lewis, et al. (2008), Multi-instrument analysis of electron populations in Saturn's magnetosphere, *J. Geophys. Res.*, 113, A07208, doi:10.1029/2008JA013098.
- Sergis, N., S. M. Krimigis, D. G. Mitchell, D. C. Hamilton, N. Krupp, B. H. Mauk, E. C. Roelof, and M. K. Dougherty (2009), Energetic particle pressure in Saturn's magnetosphere measured with the Magnetospheric Imaging Instrument on Cassini, *J. Geophys. Res.*, 114, A02214, doi:10.1029/2008JA013774.
- Sergis, N., et al. (2010), Particle pressure, inertial force, and ring current density profiles in the magnetosphere of Saturn, based on Cassini measurements, *Geophys. Res. Lett.*, 37, L02102, doi:10.1029/2009GL041920.
- Sittler, E. C., Jr., et al. (2005), Preliminary results on Saturn's inner plasma sphere as observed by Cassini: Comparison with Voyager, *Geophys. Res. Lett.*, 32, L14S07, doi:10.1029/2005GL022653.
- Sittler, E. C., Jr., et al. (2006), Cassini observations of Saturn's inner plasma sphere: Saturn orbit insertion results, *Planet. Space Sci.*, 54, 1197–1210, doi:10.1016/j.pss.2006.05.038.
- Sittler, E. C., Jr., et al. (2008), Ion and neutral sources and sinks within Saturn's inner magnetosphere: Cassini results, *Planet. Space Sci.*, 56, 3–18.
- Smith, H. T., M. Shappirio, E. C. Sittler, D. Reisenfeld, R. E. Johnson, R. A. Baragiola, F. J. Crary, D. J. McComas, and D. T. Young (2005), Discovery of nitrogen in Saturn's inner magnetosphere, *Geophys. Res. Lett.*, 32, L14S03, doi:10.1029/2005GL022654.
- Smith, H. T., R. E. Johnson, E. C. Sittler, M. Shappirio, D. Reisenfeld, O. J. Tucker, M. Burger, F. J. Crary, D. J. McComas, and D. T. Young (2007), Enceladus: The likely dominant nitrogen source in Saturn's magnetosphere, *Icarus*, 188, 356–366.
- Thomsen, M. F., and D. M. Delapp (2005), Numerical moments computation for CAPS/IMS, Los Alamos National Laboratory, *Report LA-UR-05-1542*.
- Tokar, R. L., et al. (2005), Cassini observations of the thermal plasma in the vicinity of Saturn's main rings and the F and G rings, *Geophys. Res. Lett.*, 32, L14S04, doi:10.1029/2005GL022690.
- Wilson, R. J., R. L. Tokar, M. G. Henderson, T. W. Hill, M. F. Thomsen, and D. H. Pontius Jr. (2008), Cassini plasma spectrometer thermal ion measurements in Saturn's inner magnetosphere, *J. Geophys. Res.*, 113, A12218, doi:10.1029/2008JA013486.
- Young, D. T., et al. (2004), Cassini Plasma Spectrometer investigation, *Space Sci. Rev.*, 114, 1–112.
- Young, D. T., et al. (2005), Composition and dynamics of plasma in Saturn's magnetosphere, *Science*, 307, 1262–1266.
- F. J. Crary and D. T. Young, Southwest Research Institute, San Antonio, TX 78228-0510, USA.  
D. M. Delapp, M. F. Thomsen, and R. L. Tokar, Los Alamos National Laboratory, Los Alamos, NM 87545, USA. (mthomsen@lanl.gov)  
M. A. McGraw, Tetra Tech, 2525 Palmer Street, Suite 2, Missoula, MT 59808, USA.  
D. B. Reisenfeld and J. D. Williams, University of Montana, Missoula, MT 59812, USA.  
E. C. Sittler, Goddard Space Flight Center, Greenbelt, MD 20770-2548, USA.